RSC Advances

REVIEW

Cite this: *RSC Adv.*, 2023, **13**, 18568

Prospects of 2D graphdiynes and their applications in desalination and wastewater remediation

Adrija Ghosh,[a] Jonathan Tersur Orasugh, [bc] Suprakas Sinha Ray *[bc] and Dipankar Chattopadhyay [ad]

Water is an indispensable part of human life that affects health and food intake. Water pollution caused by rapid industrialization, agriculture, and other human activities affects humanity. Therefore, researchers are prudent and cautious regarding the use of novel materials and technologies for wastewater remediation. Graphdiyne (GDY), an emerging 2D nanomaterial, shows promise in this direction. Graphdiyne has a highly symmetrical π-conjugated structure consisting of uniformly distributed pores; hence, it is favorable for applications such as oil–water separation and organic-pollutant removal. The acetylenic linkage in GDY can strongly interact with metal ions, rendering GDY applicable to heavy-metal adsorption. In addition, GDY membranes that exhibit 100% salt rejection at certain pressures are potential candidates for wastewater treatment and water reuse *via* desalination. This review provides deep insights into the structure, properties, and synthesis methods of GDY, owing to which it is a unique, promising material. In the latter half of the article, various applications of GDY in desalination and wastewater treatment have been detailed. Finally, the prospects of these materials have been discussed succinctly.

Received 28th February 2023
Accepted 5th June 2023

DOI: 10.1039/d3ra01370g

rsc.li/rsc-advances

[a]*Department of Polymer Science and Technology, University of Calcutta, Kolkata-700009, India*

[b]*Department of Chemical Sciences, University of Johannesburg, Doorfontein, Johannesburg 2028, South Africa. E-mail: suprakas73@yahoo.com*

[c]*Centre for Nanostructures and Advanced Materials, DSI-CSIR Nanotechnology Innovation Centre, Council for Scientific and Industrial Research, Pretoria 0001, South Africa. E-mail: rsuprakas@csir.co.za*

[d]*Center for Research in Nanoscience and Nanotechnology, Acharya Prafulla Chandra Roy Sikhsha Prangan, University of Calcutta, JD-2, Sector-III, Saltlake City, Kolkata-700098, WB, India*

Adrija Ghosh obtained her M.Sc. degree from Veer Surendra Sai University of Technology, Odisha. She is currently pursuing her PhD degree in Polymer Science and Technology from the University of Calcutta. Her research focuses on the various environmental and biomedical applications of nanomaterials, polymers and their composites.

Dr Jonathan Tersur Orasugh received his PhD in Nanoscience and Nanotechnology (Polymer Science and Engineering), from the University of Calcutta, India. Currently, he is working as a Postdoctoral Fellow at the Department of Chemical Sciences, University of Johannesburg and is also a senior researcher at the Centre for Nanostructures and Advanced Materials, DSI-CSIR Nanotechnology Innovation Centre, Council for Scientific and Industrial Research, Pretoria, South Africa. His research work focuses on the processing and characterization of biopolymer based immiscible polymer blends for biomedical applications, particularly drug delivery and tissue engineering.

1. Introduction

Desalination, which is typically performed using membranes, is a novel technology for addressing the global water crisis.[1,2] It is one of the most efficient methods for wastewater treatment.[3,4] Owing to their excellent resilience, high efficiency, and low production cost, graphyne (GY)-based membranes have recently received much interest for water/wastewater remediation through adsorption, catalysis, or filtration. The interest in graphdiyne (GDY) is primarily driven by the search for highly efficient carbon materials for wastewater treatment *via* desalination, filtration, or adsorption.

Carbon performs a specific role in every known life-form. In addition to the important naturally occurring "bulk" allotropes such as diamond and graphite (sp^2-hybridized), carbon exists in many low-dimensional forms. Fig. 1 shows various carbon allotropes composed of different hybridized carbon atoms. The discovery of fullerenes,[5] carbon nanotubes (CNTs),[6] and graphene (Gra)[6–8] has led to advancements in science and technology. These materials possess unique physical, structural, mechanical, and chemical properties. Unlike sp^2-hybridized carbon atoms, purely sp-hybridized carbon atoms can form only one structure: the linear allotrope, carbyne.[9] Unique, synthetic allotropes can be prepared by linking sp^2- and sp-hybridized carbon atoms; examples of such allotropes include GY,[10] GDY,[11,12] and their derivatives.

Diamond and graphite, which have long networks of sp^3- and sp^2-hybridized carbon atoms, respectively, are the two primary naturally occurring carbon allotropes.[14] The discovery of fullerenes, carbon nanotubes, and Gra has broadened the categories of existing sp^2-hybridized carbon compounds. In theory, the flexibility and adaptability of carbon atoms with respect to their diverse hybrid structure(s) allow for the synthesis of carbon allotropes *via* the alteration of the periodic motifs within the networks of sp^3-, sp^2-, and sp-hybridized carbon atoms.[15] The carbon allotrope, GY, which consists of layers of assembled sp- and sp^2-hybridized carbon atoms, is a synthetically feasible carbon allotrope.[15] Its name "graphyne" originates from its resemblance to graphite and the presence of acetylenic components. Graphyne is a layered planar material consisting of hexagonal rings and acetylenic linkages.[16] Haley *et al.* proposed the preparation of GDY, which has two diacetylenic linkages between recurring patterns of carbon hexagons.[11,15] Both sp- and sp^2-hybridized carbon atoms are present in the networks of GDY and GY, which could be compared to the hybrid systems of Gra and carbyne,[11] as depicted in Fig. 1. The members of the GDY and GY families possess an extensive π-conjunction, uniformly distributed pores, and tunable electronic characteristics owing to the flat (sp^2- and sp-hybridized) carbon networks. Their application potential has been demonstrated experimentally: they hold great promise as energy-storage systems, gas-separation membranes, and battery anodes.

Plain carbon (sp^2 and sp) linkages endow the GDY and GY families with uniformly distributed pores, high degrees of π-conjunction, and tunable electronic properties. Thus, these materials attract significant attention from structural, theoretical, and synthesis scientists who aim to harness their promising electronic, optical, and mechanical properties. The traditional sp^2-hybridized carbon systems fullerenes, nanotubes, and Gra along with the 0D, 1D, and 2D forms of GDYs and GYs are suitable for various applications and can address the growing demand for carbon nanomaterials.

Professor Suprakas Sinha Ray obtained a PhD in Physical Chemistry from the University of Calcutta in 2021. He is a Chief Researcher at the Council for Scientific and Industrial Research and Manager of the Centre for Nanostructures and Advanced Materials and Director of the DSI-CSIR Nanotechnology Innovation Centre. He is also associated with the University of Johannesburg as a distinguished visiting Professor of Chemical Sciences. Ray's current research focuses on polymer-based advanced nanostructured materials and their applications.

Prof. (Dr) Dipankar Chattopadhyay is the former head of department and Professor of the Department of Polymer Science and Technology, University of Calcutta, 92 A.P.C. Road, Kolkata-700 009, India. He is an experienced, resourceful and well-published teaching and research professional with expertise in polymer science and technology: synthesis and characterization, polymer nanocomposites, hydrogel-based biomaterials, rubber compounding and technology, conducting polymers and has the initiative to develop creative solutions to a broad range of research problems in the above fields. He is an experienced and knowledgeable research professional in the development of advanced polymers and nanomaterials with special emphasis on biodegradable, biocompatible advanced polymers and nanomaterials obtained through the dictates of green chemistry and green technology to meet the challenges of today's society.

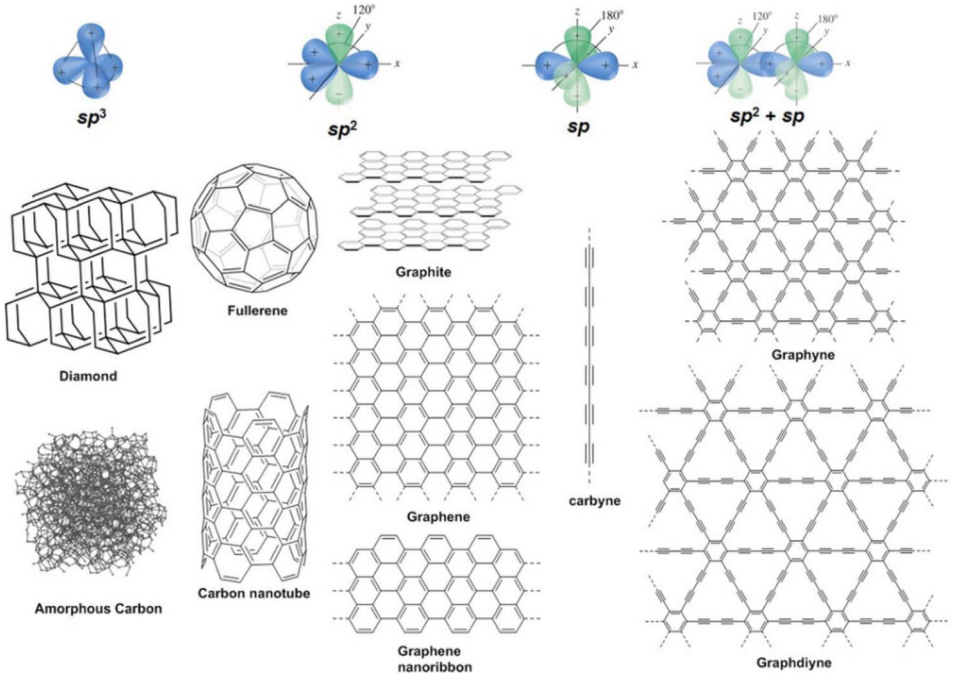

Fig. 1 Various carbon allotropes composed of different hybridized carbon atoms. Reproduced with permission from Chen *et al.*[13] Copyright 2017, Wiley.

According to various theories, including exchange–correlation functionals, GY and GDY have a more complex electronic structure than Gra, possessing features such as anisotropy, nonequivalent Dirac points, and a noticeable band gap (BG) of 0.46–1.22 eV.[17] They could exhibit chemical and physical adaptability, similar to Gra, owing to their homogeneous pores and chemically active triple bonds. Therefore, theoretical studies have predicted unique electronic,[18,19] optical,[20] and mechanical properties[21,22] of Gys and GDYs that would render them applicable to transistors, hole-transport systems, field-emission devices, desalination membranes,[1,23–25] batteries, gas-separation membranes,[26,27] catalysts,[28,29] and sensors.[30,31]

Gradually, graphdiyne is being increasingly used in water desalination and wastewater remediation.[1,23–25] This review, for the first time, reports the applications of GDY in desalination and wastewater treatment as a stand-alone paper for the first time. An in-depth introduction to GDY and GY and the diverse synthesis methods for GDY are presented. The properties of GDY, current challenges, conclusions, and future outlook on the synthesis and applications of GDY are discussed in detail based on the literature, with the aim of broadening the understanding of the related topics.

2. GDY and its history

'The history of the GY/GDY family (sp^1 + sp^2) of carbon allotropes can be categorized into two phases. In 1987, Baughman *et al.*[32] presented the first structural examples of Gys and several macrocyclic subunits appropriate for constructing their 2D networks. Their study marks the beginning of the first phase. In 1997, Haley, Brand, and Pak synthesized GDYs; this study represents a significant advancement in the group of (sp^1 + sp^2) allotropes.[33]

The first-principles simulations of 0D,[34] 1D,[35] and 3D GY- and GDY-like materials[36] and their B–N and B–C–N analogs[37–39] were performed. The development of the two main types of (sp^1 + sp^2) single-atom-thick networks (Gys) and the experimental efforts to synthesize their constituents 'are largely attributed to their organic chemistry, especially to the novel synthesis methods in annulene chemistry.[40] This growing interest marks the beginning of the second phase (typically in 2008), involving extensive experimental and theoretical studies on Gra and Gra-based materials.

Numerous experimental advances have been achieved in the last decade: preparation of large-area semiconducting GDY membranes on the Cu surface *via* a cross-coupling-based reaction using hexaethynylbenzene (HEB);[41] fabrication of high-conductivity, high-mobility GDY nanowires (GDNWs) as novel electronic and photoelectric systems;[42] and application of GDYs as components of polymer solar cells[43] and photocatalyst nanocomposites.[44] In 2012, Li *et al.*[45] reported the fabrication of graphdiyne nanotube (GDNT) arrays using a Cu-catalyzed anodic Al_2O_3 template.

However, the following shortcomings are noted: (a) these experiments[44,46] were reported by a single research group (Yongjun Li *et al.*), necessitating an additional, independent verification, (b) only GDYs have been synthesized in these studies, and (c) the preparation of Gys has not been reported. Currently, theoretical studies have substantially outpaced experimental studies, offering a promising outlook on prospective areas for studying these materials. For instance, it was predicted by Malko *et al.*[47], and Cui *et al.*[48] that some GY and

GDY networks would exhibit excellent electrical properties, rendering them more adaptable than Gra owing to anisotropy and the presence of nonequivalent Dirac points. Additionally, the mechanical characteristics of some Gys and GDYs (free-standing/hydrogenated)[18,49] have been determined. The nonlinear stress–strain behavior was attributed to the distinctive atomic configuration in GY; moreover, the acetylenic functionalities afforded tunable resilience.[49] The in-plane stretching could result in a mechanically stimulated phase transition from Gra to GDY.[50,51] Therefore, these systems are promising materials for nanoelectronic devices, energy-storage modules, battery anodes,[51,52] hydrogen-storage units,[53] and gas-separation membranes.[54] In addition, the application potential of Gra and GY sheets and ribbons has expanded significantly. Researchers have investigated the modification of the characteristics of pure Gra sheet: the adsorption of 3D atoms to GY and GDY sheets facilitates their magnetization. For example, V/GY, Mn/GY, and Fe/GY can act as a magnetic half-metal, spin-selective half-semiconductor, and magnetic metal, respectively.[55] The stoichiometries of fluorographynes (fluorinated Gys) such as C_2F_3 (F/C = 1.5), C_3F_5 (F/C = 1.66), and C_4F_7 (F/C = 1.75) have been postulated and studied.[56]

Balaban *et al.*'s work in 1968 (ref. 57) offered initial insights into a wide variety of planar carbon networks entirely composed of sp^2-hybridized carbon atoms with a triple coordination. The subsequent studies in this research direction led to the construction of multiple associated 2D periodic carbon networks from non-C_6 carbon polygons. Some related types of carbon networks (termed as Gra allotropes)[58,59] have been proposed and investigated, pentaheptites,[60] Haeckelites[61] (such as C_5, C_6, and C_7), and the family of possible 2D atomic motifs of GY-like structures, as shown in Fig. 2. These hypothetical low-stable polycyclic networks comprise strained cycles such as C_3, C_4, and C_{12}; their synthesis method remains to be known. This category also includes the latest 2D square carbons.[62]

Graphynes and graphdiynes are prepared by replacing some ═C═C═ bonds in Gra with acetylenic (–C≡C–) or diacetylenic (–C≡C–C≡C–) linkages *via* an alternative approach for obtaining flat single-atom-wafer-thick carbon networks.

The conventional synthesis methods of diverse GY/GDY-based materials have been reported. This review is focused on developing simpler, more cost-effective, and more eco-friendly approaches, through which high-efficiency synthesis methods can be discovered. In addition, this paper aims to facilitate the synthesis of application-specific GY/GDY-based materials, thereby leading to highly functional and effective systems for advanced applications.

2.1. Structure of GDY

2.1.1. From Gys as the fundamental building blocks of GDY. Graphyne is an unconventional type of a flat carbon network with sp^1 and sp^2 hybridized carbon atoms, as proposed by Baughman *et al.*[32] Various Gra-like network types are possible, *e.g.*, by substituting some (or all) carbon–carbon double bonds in the aforementioned sp^2-hybridized Gra-like allotropes with acetylenic linkages (–C≡C–).

These and related networks can be categorized into four major groups: I through IV (see Fig. 2). C_6 hexagons that are joined by –C≡C–linkages constitute Group I (GY1). C_6 hexagons and pairs of sp^2-hybridized carbon atoms (C═C bonds) are present in the two networks of Group II (GY2 and GY3) connected by –C≡C– linkages. The three Group III networks (GY4–

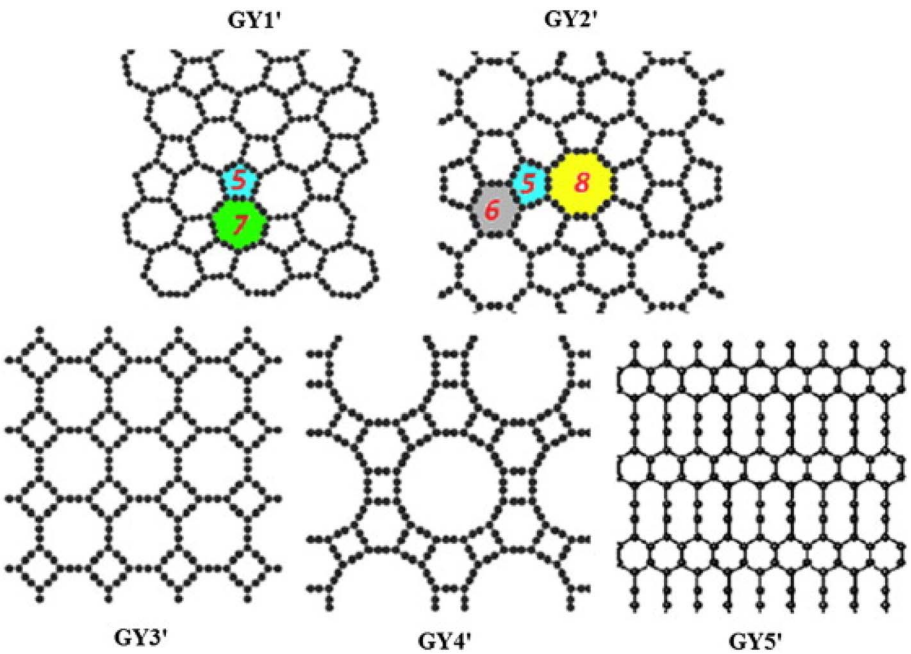

Fig. 2 Some possible atomic motifs of GY-like structures, which have been assigned the terminologies GY1′–GY5′ in the text. Reproduced with permission from Ivanovskii,[17] Copyright 2013, Elsevier Science Ltd.

GY6) comprise only pairs of sp^2-hybridized carbon atoms (= bonds) joined together by –C≡C– linkages (GY4 and GY5) or pairs of sp^2-hybridized carbon atoms and solitary sp^2-hybridized carbon atoms (GY6). The network of Group IV consists of only solitary sp^2-hybridized carbon atoms connected by –C≡C– linkages (GY7). All the C= bonds in this network (referred to as super-Gra) are replaced by acetylenic linkages or carbon–carbon triple bonds; hence, their structure resembles that of Gra. Therefore, both GY7 and Gra exhibit hexagonal *p6m* symmetry.

The aforementioned systems have not been uniformly categorized to date. To denote the GY networks investigated in their work, Baughman *et al.*[32] abridged the nomenclature that specifies the number of carbon atoms in various rings that constitute a particular network. For instance, the super-GY (GY7) and

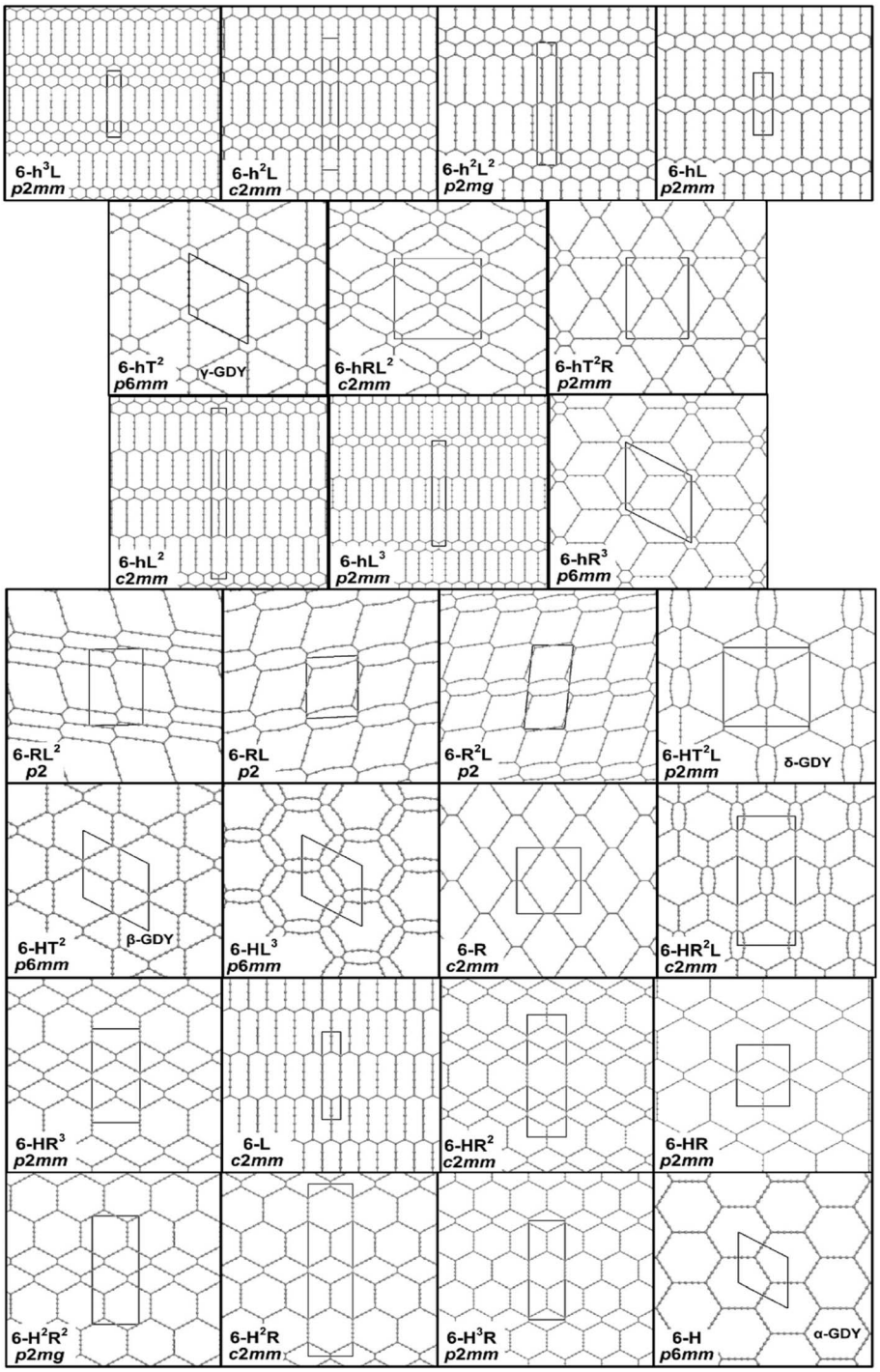

Fig. 3 Representation of the 26 2D structures identified and investigated in this work. The unit cells and plane groups are indicated. α-, β-, γ-, and δ-GDYs are labeled. Reproduced with permission from Sarafini *et al.*[65] Copyright 2021, ACS Publications.

GY2 networks were named 18,18,18-GY and 6,6,14-GY, respectively. In addition, GY-like networks have been assigned alternative names:[63] α-GY is the term given to the structure GY7 (ref. 63) and γ-GY to the GY1.[64]

Regarding the different types of GYs, the structures of GY1′ and GY2′ (Fig. 2) could be constructed from pentaheptite/Haeckelite structural architectures by replacing all carbon–carbon double bonds with acetylenic linkages (carbon–carbon triple bonds). The structures of GY3 and GY4′ are GY-like analogs of some 2D carbon supracrystals. Several Gra/GY hybrids are feasible as well. For example, GY5′ consists of stripes of C_6 hexagons joined together by acetylenic linkages such as carbon–carbon triple bonds.

The abovementioned examples infer that the atomic structures of different potential GYs significantly impact the relative stability and characteristics of those compounds as depicted in Fig. 2 and discussed in the previous paragraph.

In all GYs, the sp^2-hybridized atoms are connected by an individual carbon–carbon triple linkage. Therefore, an additional method of constructing GY-like networks is to lengthen the linear carbine-like atomic chains that connect the sp^2-hybridized atoms, that is, by replacing (–C≡C–) chains with (–C≡C–C≡C–) or (–C≡C–C–C–C≡C–) chains that link either C_6 hexagon sets of the group of the purported GDYs. This approach has historically been taken into consideration, taking into account its straightforwardness: the approach is also independent of the extremely wide range of potential GY-like ($sp^1 + sp^2$) networks. The initial representation of GDY was proposed in 1997.[33] Serafini *et al.*[65] postulated 2D structural architectures of GDY, as shown in Fig. 3. These structures can generally be categorized as GY networks, wherein all acetylenic linkages are modified into diacetylenic linkages, such as −C≡C–C≡C−. Owing to the substitution of acetylenic linkages by diacetylenic linkages, the term "graphdiyne" is derived from the term "graphyne".[32] Furthermore, a wide variety of GDYs is feasible, similar to that of GYs; Gra/GDY, GY/GDY, Gra/GY/GDY, and other exotic hybrids have also been postulated.

Recently, the construction of monomeric and oligomeric subunits consisting of carbon atoms with hybridizations similar to sp^1 and sp^2 has advanced significantly. These subunits can be used for preparing the abovementioned GY and GDY sheets (Fig. 4). The related data have been reported in several recent studies,[66,67] serving as the experimental foundation for GY and GDY synthesis.

In conclusion, GYs coupled with acetylene linkages have been extensively investigated as building blocks of GDYs. Furthermore, it would be imperative to use materials that can be modified through chemical engineering and process control engineering to optimize the production cost, processing time, and environmental friendliness of the synthesized material.

Recently, Li *et al.* fabricated large-area GDY films for the first time,[41] wherein the GDY films were prepared on the Cu surface *via* a cross-coupling reaction with HEB. The GDY multilayers constituted the prepared GDY films, which were uniform. The electrical characterization of these films inferred their excellent semiconducting behavior; their electrical conductivity (EC) varied from $\sim 2.516 \times 10^{-4}$ S m^{-1} (GDY thin film)[69] to $\sim 1.9 \times 10^{3}$ S m^{-1} (GDNWs),[42] and their thermal conductivity (TC)[70,71] varied from ~7.22 to 7.30 W mK^{-1}, respectively, at ambient temperature. The TC of 2D GDY was isotropic in the armchair and zigzag planes, measuring 50 W mK^{-1};[72] however, upon downsizing the 2D GDY into nanoribbons (Fig. 5a–d), the TC became anisotropic and significantly decreased to 28.0 W mK^{-1} (armchair plane; Fig. 5a) and 18.2 W mK^{-1} (zigzag plane; Fig. 5a) because of strong photon boundary scattering.[72]

2.1.2. Structure of GDY. Graphdiyne is mainly synthesized from repeated structural linkages of GY containing sp^2- and sp-hybridized carbon atoms joined together. Graphyne is prepared by inserting acetylenic linkages (referred to as sp-hybridized carbon atoms) into the pristine honeycomb architecture of

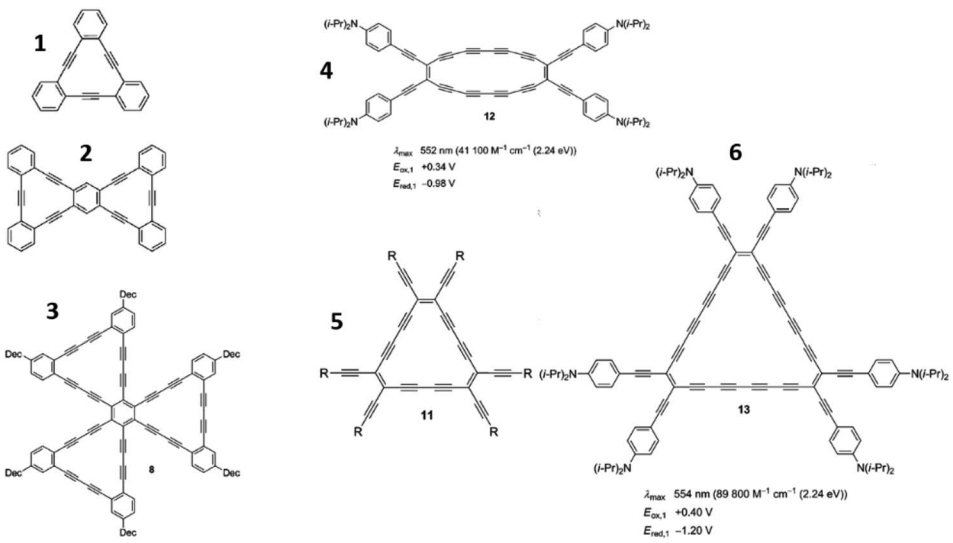

Fig. 4 Selected structures of synthesized benzannellated dehydroannulene-based molecules (1–3) and perethynylated dehydroannulene-based molecules (4–6) as building blocks for GY- and GDY-sheet synthesis. Reproduced with permission from Diederich and Kivala.[68] Copyright 2010, Wiley.

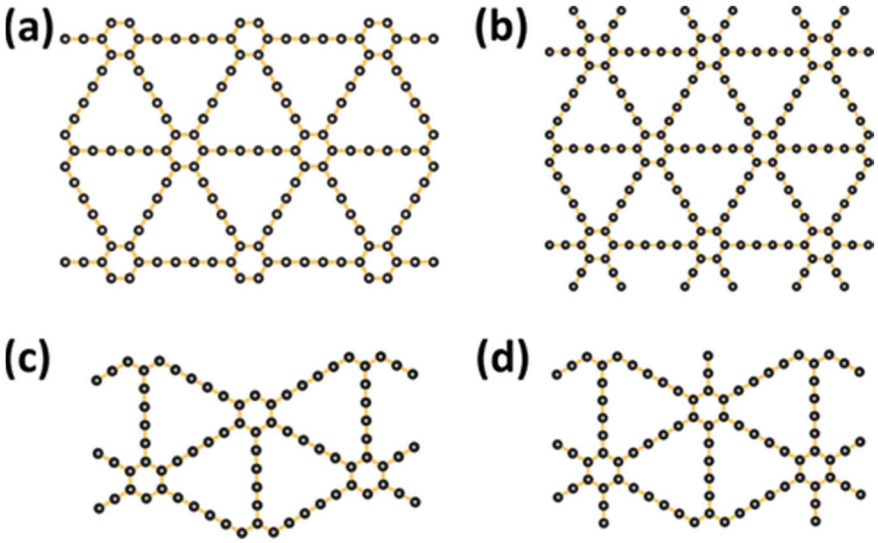

Fig. 5 Schematic of the simulated nanoribbon structures. Structures (a) and (c) are nanoribbons in the armchair and zigzag directions, respectively. Structures (b) and (d) are constructed based on structures (a) and (c), respectively, by adding side chains onto the edges. Reproduced with permission from Wan *et al.*[72] Copyright 2019, American Chemical Society.

Gra, which consists of sp^2-hybridized carbon atoms, as depicted in Fig. 6. Accordingly, α-, β-, and γ-GYs are synthesized by incorporating acetylenic linkages between all the carbon atoms (Fig. 6a), pairs of sp^2-hybridized carbon atoms (Fig. 6b), and aromatic rings of the vertices Fig. 6c. Therefore, the structures of α-, β-, and γ-GYs consist of 100%, 66.67%, and 33.33% acetylenic groups, respectively. The coordination number of Gra is 3; however, GYs have non-integer average coordination numbers: the average coordination numbers of α-, β-, and γ-GYs are 2.25, 2.33, and 2.50, respectively.[73]

The unique structural, optical, thermal, mechanical, and electrical properties of GY, which is a single-atom-thick carbon allotrope, are attributed to its acetylenic linkages.[74] Its characteristics such as large pores, low fracture stress, and high Young's modulus drastically differ from those of Gra[75] owing to the presence of Dirac cones and BGs at the Fermi level. Thus, these materials must be readily synthesized to expand the range of their potential applications. For Gra, only a few key components have been prepared using graphite flakes;[76] however, for GDY, the cross-coupling process on a copper foil facilitates the assembly of large-area ordered membranes using HEB.[41] Their structural,[77,78] mechanical,[79–81] and electrical[66,82–84] properties have been widely studied in the past few years using first-principles electronic-structure calculations. Hence, GYs have emerged as prospective candidates for use as energy-storage materials,[25] catalysts,[85] ultraviolet-light shields,[86] transistors,[87] anode materials in batteries,[88] and transistor anodes.

In summary, the structures of GY/GDY and GY- and GDY-based materials have been primarily postulated by researchers using structural modeling software and secondarily using instruments or analytical machines. However, the reliability of these models without backup experimental data and results remains uncertain. The structural predictions and calculations must be ascertained by experimental results for their definitiveness.

2.2. Properties of GDY

2.2.1. Structure and comparative stability. Ivanovskii *et al.*[17] used several computational methods and thoroughly explored equipoise atomic architectures (lattice factors and interatomic gaps) of 2D single-atom-thick systems of hexagonal GY (GY1) and GDY, as depicted in Fig. 7, which was obtained by another research group;[89] the results were similar (Table 1). The lengths of the carbon–carbon bonds in C_6 hexagons and

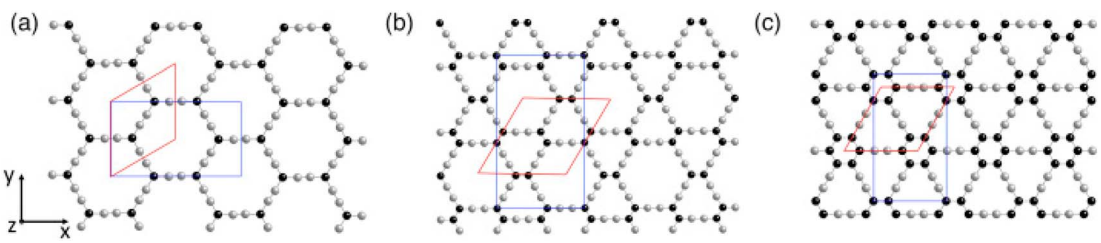

Fig. 6 (a) α-, (b) β-, and (c) γ-GY structures maintaining the armchair direction along the *x*-axis and the zigzag direction along the *y*-axis with sp- and sp^2-hybridized carbon atoms depicted in grey and black, respectively. Rhombohedral (red) and rectangular (blue) unit cells are also shown. (A colored version of this figure can be viewed online.) Reproduced with permission from Puigdollers *et al.*[73] Copyright 2016, Elsevier Science Ltd.

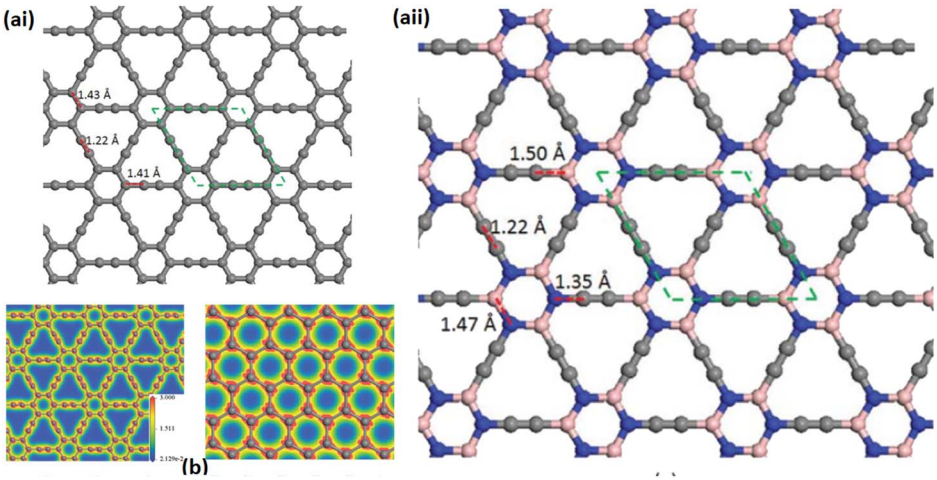

Fig. 7 (a) Geometric structure of optimized GY. The unit cell is represented using green dashed lines. (b) Contour plots of total electron density of GY (left panel) and Gra (right panel) for comparison. Reproduced with permission from Zhou *et al.*[89] Copyright 2011, American Institute of Physics.

Table 1 Lattice constants (*a*, in Å) and band gaps (BGs, in eV) of hexagonal GY (GY1) and Gra based on the theoretical information in the literature. Reproduced with permission from Ivanovskii.[17] Copyright 2013, Elsevier Science Ltd

Network	GY1	GDY
a	6.86[a,b]; 6.89[c]; 6.889[d]; 6.86[f]; 6.90[j]	9.44[b]; 9.464[d]; 9.48[h]; 9.37[i]
BG	1.2[a]; 0.52[b]; 0.46/0.96[c]; 0.47/2.23[d]; 0.47[j]	0.53[b]; 0.52/1.18[d]; 1.22[e]; 044/1.10[g]; 0.46[h]; 0.53[i]

[a] Ref. 10, MNDO. [b] Ref. 78, FP-LCAO. [c] Ref. 91, VASP-PAW: GGA-PBE/HSE06. [d] Ref. 50, VASP: GGA-PBE/Crystal06: B3LYP. [e] Ref. 92, hybrid exchange–correlation functional. [f] Ref. 93, DMol3. [g] Ref. 94, ABINIT-YAMBO: LDA/G. [h] Ref. 19, VASP-PAW: GGA/PBE. [i] Ref. 95, CASTEP: GGA/PBE. [j] Ref. 96, VASP.

acetylenic or diacetylenic linkages are not uniform, indicating various bonding types for each pair of carbon atoms such as =C=C=, –C=C–, =C–C≡, and ≡C–C≡ (see Fig. 6 and 7). Unlike Gra, the GYs, GDYs, and other related (sp^1 + sp^2) networks exhibit significant structural flexibility owing to the diversity of C–C bonds. In particular, this diversity will result in temperature-dependent rippling of these flat networks or a reduction in their mechanical stiffness. The ionic contribution to chemical bonding or the partial electron transfer between C_6 rings and sp^1-hybridization-like atoms produces an additional effect; however, the direction of such a charge transfer has not been determined yet.[89,90]

The –C–C– bond lengths in C_6 hexagons and acetylenic or diacetylenic linkages are not uniform, indicating various bonding categories for individual pairs of carbon atoms such as =C=C=, –C≡C–, =C–C, and C–C, shown in Fig. 7.[89] This diversity of carbon–carbon bonds results in significant structural flexibilities of GYs, GDYs, and other related sp^1 + sp^2 networks, unlike Gra, and leads to temperature-dependent rippling of the flat networks or a reduction in their mechanical stiffness. The diversity of –C≡C– bonds is attributed to the different types of sp^1- and sp^2-like atomic hybridization. The partial electron transfer between C_6 rings and sp^1-hybridization-like atoms or the contribution of ionic impact to chemical bonding results in an additional effect; however, the direction of this type of charge transfer has not been determined yet.[89,90]

Such structural irregularities can be advantageous for different atomic switches or the development of curved structural molecules such as nanotubes.

Unlike the stabilities of Gra and several other sp^2-hybridization-like Gra allotropes, the stability of 2D carbon networks is decreased by the presence of acetylenic or diacetylenic linkages (*i.e.*, sp^1-hybridized atoms). In Fig. 8, the equations of state (EOSs) for four alternative sp^2-hybridization-like 2D carbon networks are shown, relative to that of GDY,[90] to substantiate this fact. Graphdiyne is the most energetically volatile material.

The relative stabilities of GYs and GDYs have been widely investigated. The semi-empirical MNDO calculations by Baughman *et al.*[32] in 1987 estimated the gas-phase development energies for a set of GYs. The measured Heat of formation (H_f) values (in kcal mol^{-1}) of the GYs under consideration exhibited the following order: 14.9 (6,6,6) < 17.8 (6,6,12) < 19.3 (6,6,14) < 23.7 (14,14,1 4) ≈ 23.7 (12,12,12) < 25.2 (14,14,18) < 26.3 (18,18,18). This observation implies that the stability of GY-like networks decreases with increasing number of sp^1-hybridized atoms or acetylenic linkages (–C≡C–).

For these estimates, the variations in the total energies E_{tot} (ΔE_{tot}) between the 2D networks under consideration and Gra (the most stable 2D carbon) were considered. In addition, the cohesive energy, E_{coh}, which is the difference between the total energy of the system and the sum of total energies of the constituent atoms, is commonly used to measure the strength of the forces that hold atoms together in crystals. Narita *et al.*[97] showed that GY1 was more stable than GDY with ΔE_{tot} ≈ 0.17 eV $atom^{-1}$.

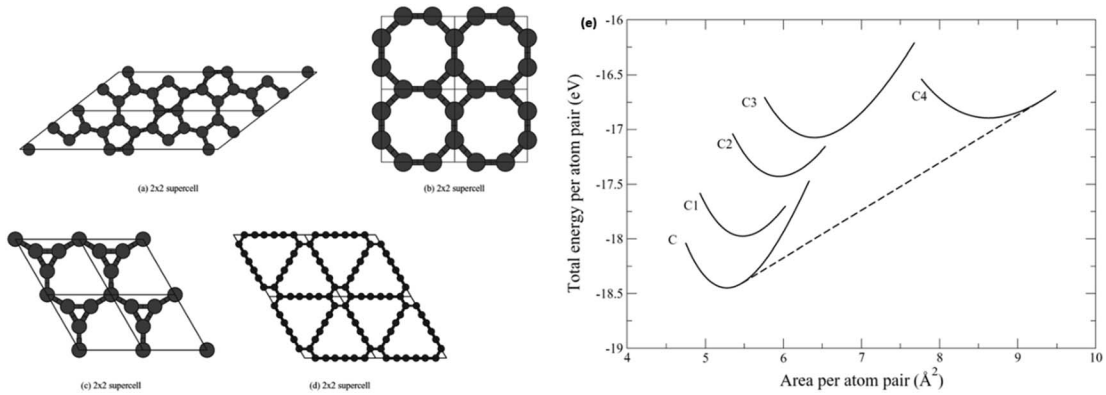

Fig. 8 Four Gra allotropes: (a) C1 (pentaheptite) consisting of pentagons and heptagons, (b) C2 consisting of squares and octagons, (c) C3 consisting of triangles and enneagons, and (d) C4 (GDY) consisting of two acetylenic linkages between hexagons. EOSs for Gra and four allotropes revealing the phase transition from Gra to C4 at $F = -7.0$ N m^{-1}. Reproduced with permission from Andrew *et al.*[90] Copyright 2012, APS. (e) EOS for graphene and four allotropes showing a phase transition from graphene to C4 at $F = -7.0$ N m^{-1}.

The computed Gibbs free energy, ΔG, of GDY[93] is 0.803 eV atom^{-1} (same as that of Gra); the ΔG of diamond, graphite, (6,6) nanotube, fullerene C60, and carbyne are −0.022, −0.008, 0.114, 0.364, and 1.037 eV atom^{-1} respectively. The stability of successive (sp^2 + sp^1)-like 2D carbon networks decreases with increasing ratio of sp^1-/sp^2-hybridized atoms, that is, as the proportion of C=C bonds decreases, based on similar estimations[98] of ΔG (or E) using the DF-TB technique. The hypothetical hybrid structure (5) is the most stable structure (Fig. 9); it is composed of fragments of Gra and GY networks and has stripes of connected C_6 rings. The two C_6 rings that constitute GY and GDY are situated at the center of this hierarchy. Finally, the lowest stability pertains to network (4), referred to as super-Gra, which consists exclusively of isolated sp^2-hybridized carbon atoms connected by acetylenic linkages. The stability further decreases for network (3) containing separate pairs of C(sp2)=C(sp^2) bonds.

2.2.2. Electronic properties. The unique features of Gra are attributed to its exceptional electrical properties, especially the gapless band structure with 2D Dirac-like electronic excitations.[100] The electronic structure of Gra single networks and hexagonal GY (GY1) has been widely studied using various computational methodologies.[48,89,90] Unlike Gra, GY1 and GDY are semiconductors that undergo direct transitions at the M points of the Brillouin zone. Based on the methods employed and the exchange–correlation functionals used, their minimum BG ranges from 0.46 to 1.22 eV.

The deep σ-type bands in the spectra of GY, GDY, and GY1 are relatively similar;[101] the low-energy π (π*) bands form the edges of the BG.

Malko *et al.*[47] predicted that some GY-like networks may exhibit exceptional charge-transport capabilities and that GY may surpass Gra.[102] Malko *et al.*[47] showed that the Dirac-cone-like feature was not a unique property of G and that it was independent of the hexagonal symmetry and honeycomb structure of the carbon sheets. Therefore, the electrical band structures of the three GYs were examined. The first two GYs exhibited Dirac-cone-like properties when the valence and conduction bands overlapped at a single location near the Fermi level ($E_F = 0$ eV). Owing to the hexagonal symmetries, the electrical characteristics of these networks did not exhibit strong anisotropy in their plane. In general, hexagonal symmetry is a necessary condition for the existence of Dirac cones; however, the band structure of the GY-like network, which exhibits rectangular symmetry (*pmm*), consisted of four Dirac points (as two pairs) in the Brillouin zone. These two types of Dirac points were formed by the orbitals of various carbon atoms, denoting unique anisotropic electrical properties, especially new ECs.[47] Latest first-principles calculations have demonstrated that Gra subjected to asymmetric uniaxial tensile strain[48] and rectangular 2D GY-like networks doped with BN or H2 units[103] may contain Dirac points. Hence, aside from carbon systems, a diverse range of 2D materials with different chemical compositions may exhibit unique electronic properties similar to G.

In addition, the optical spectra of a few GYs have been assessed; they exhibited considerable anisotropy. The optical adsorption was relatively weak for out-of-plane polarization in the low-energy range but strong for in-plane polarization.[91]

2.2.3. Mechanical characteristics. A few significant concerns related to the mechanical characteristics of GYs and GDYs are currently being discussed:[90,91,104]

(a) the extent to which mechanical deformations can change the properties of these networks;

(b) the process by which these networks break down under strain; and,

(c) the relationship between the elastic parameters and temperature.

In accordance with literature, the elastic parameters of GYs and GDYs independent elastic constants (C_{ij}), in-plane Young's modulus (Y; in-plane stiffness), Poisson's ratio (ν), 2D shear modulus of Gra, and layer modulus (γ; the 2D equivalent of the bulk modulus that determines the resistance of the material to hydrostatic stretching) were estimated (Table 2).[48,91] Additionally, the aforementioned parameters were specified[90] in terms of

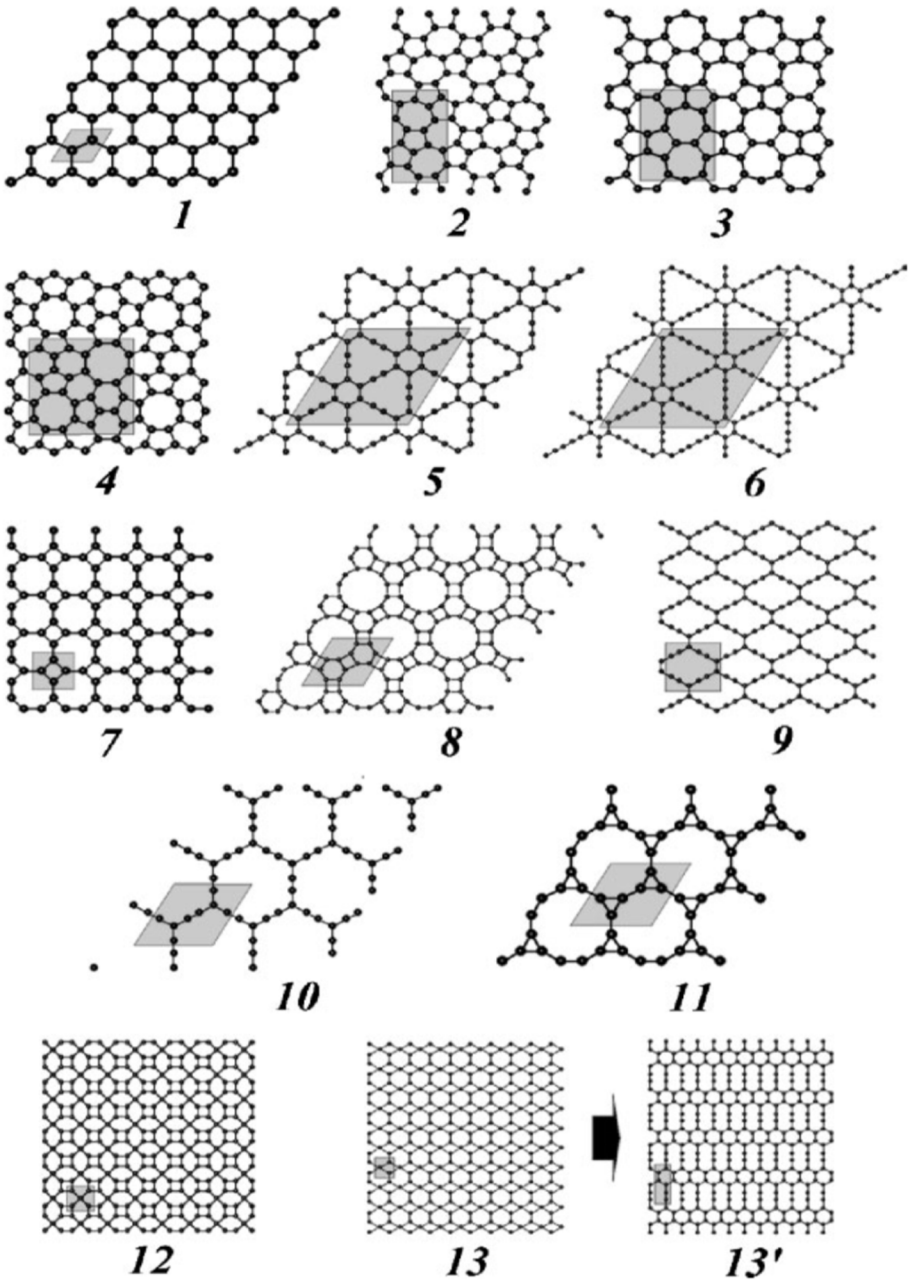

Fig. 9 Optimized atomic structures of the examined Gra allotropes (13′ – see the text). Unit cells are painted. Reproduced with permission from Enyashin *et al.*[99] Copyright 2010, WILEY-VCH Verlag GmbH & Co. KGaA, Weinheim.

independent elastic constants (for hexagonal networks, $C_{11} = C_{22}$ and C_{12});

$$Y_{[10]} = Y_{[10]} = \frac{\left(C_{11}{}^2 - C_{12}{}^2\right)}{C_{11}}; v_{[10]} = v_{[10]} = 1/2(C_{12}/C_{11}); \text{and } G = 1/2(C_{11} + C_{12}).$$

The maximum in-plane stiffness of graphene is 340–366 N m^{-1}, which decreases for GY (170–240 N m^{-1}) and GDY (~120 N m^{-1}). Consequently, the Poisson's ratios increase in the same order because[90,104] unlike the highly compact structure of Gra, the long acetylenic and diacetylenic linkages in GY and GDY, respectively, cause gradual structural weakness (*i.e.*, a decrease in the atomic bond energy, which loosens the structures), with the degree of reduction being proportional to the percentage of linkages.[107] Calculations[108] also corroborate the fact that GDY is softer than GY.

The bending stiffness of GDY was predicted to be 1.68 eV, comparable to that of Gra (1.4–1.5 eV).[49] This bending flexibility of Gra is suggestive of the potential production of nanotubes based on Gra, as shown below (Section 2.2.3). As the temperature increased from −273.15 °C to 926.85 °C (0 to 1200 K), the Young's modulus and C_{11} of GYs decreased by 24.6% and 24.8%, respectively, more significant than those of Gra (3.5% and 4.5%,

Table 2 Comparison of elastic parameters of hexagonal GY and GDY and *G*: elastic constants (C_{ij}, in N m^{-1}), Young's modulus (*Y*, in N m^{-1}), Poisson's ratio (ν), shear modulus (*G*, in N m^{-1}), and layer modulus (γ, in N m^{-1}). Reproduced with permission from Ivanovskii.[17] Copyright 2013, Elsevier Science Ltd

Parameter	Gra	GY	GDY
$C_{11} = C_{22}$	352.7[b]; 358.1[c]; 372.2[d]	239.0[e]	152.1[b]
C_{12}	60.9[b]; 60.4[c]; 46.6[d]	64.5[e]	69.0[b]
Y	342.2[b]; 348[c]; 366.4[d]	170.4[f]; 166[g]; 239.0[e]	120.8[b]
ν	0.173[b]; 0.169[c]; 0.125[d]	0.417[g]	0.454[b]
G	145.9[b]; 148.9[c]; 162.8[d]	87.3[a]	41.6[b]
γ	206.8[b]; 209.3[c]; 209.4[d]	151.8[a]	110.6[b]

[a] Calculated using the elastic constants provided in ref. 19. [b] Ref. 90. [c] Ref. 105. [d] Ref. 106. [e] Ref. 104. [f] Ref. 49. [g] Ref. 91.

respectively).[109] Consequently, the mechanical properties of GYs substantially degraded as the temperature increased, in contrast to Gra, which could maintain excellent mechanical qualities even at high temperatures. Moreover, GDYs may undergo a more significant temperature-induced deterioration of mechanical characteristics, which is yet to be determined.

The BGs of GYs and GDYs can be tuned under strain:[91] the BG of GYs increased with increasing tensile strain but decreased with increasing compressive strain.[91]

The aforementioned values are accurate within the elastic limit. Recent works have atomistically investigated the breakdown of the GY network under uniaxial tension (uniaxial tension $\Delta\varepsilon$).[49] The GY network was subjected to two uniaxial tensile tests,[49] and the stretching in the *x* and *y* directions, which differ based on the orientation of –C≡C– linkages (Fig. 10), was simulated.

The stress–strain curves in Fig. 10 reveal that the direction of the applied tension determines the point at which the GY network begins to break down ($\Delta\varepsilon_x \approx 0.08$ and $\Delta\varepsilon_y \approx 0.13$). This is because unlike $\Delta\varepsilon_x$ (tension along the –C≡C– linkages), which decreases the strain capacity of the GY network, $\Delta\varepsilon_y$ has a more uniform strain distribution over all the carbon–carbon bonds in the GY network.

Zhang *et al.*[107] compared four distinct GY networks with Gra and investigated their elastic limits. They concluded that the number of acetylenic linkages determined the extent to which the

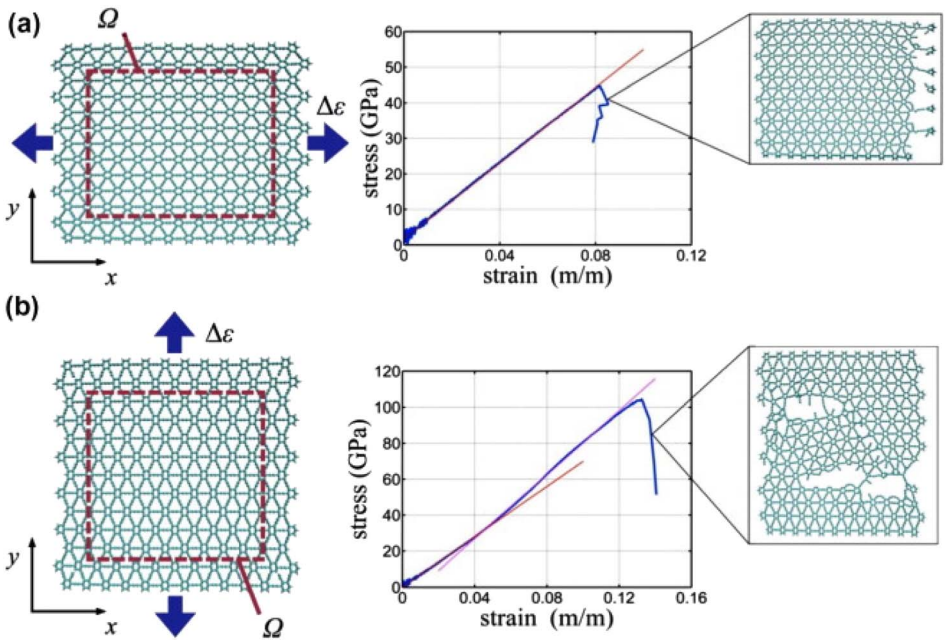

Fig. 10 Schematic and stress–strain results of uniaxial tension tests, in reclined-chair (*x*-axis) and zigzag (*y*-axis) directions. (a) Reclined-chair direction; uniform strain was applied by displacing the graphyne edges in the *x*-direction at a constant velocity. The virial stress is calculated over a representative volume, Ω, chosen within the interior of the graphyne sheet to avoid boundary effects. For volume calculations we assume a thickness of 3.20 Å, taken from adhesion energy results (Fig. 3 in Buehler[49]). Fitting the resulting stress–strain data, a Young's modulus of 532.5 GPa is calculated (or 170.4 N m^{-1} without consideration of the sheet thickness), with an ultimate stress of 48.2 GPa and maximum strain of 0.0819. Failure is found to be localized to a single edge. (b) Zigzag direction; uniform strain is applied by displacing the graphyne edges in the *y*-direction at a constant velocity. As before, the virial stress is calculated over the same representative volume, Ω, assuming a thickness of 3.20 Å (Fig. 3). Fitting the resulting stress–strain data, an initial stiffness of 700.0 GPa is calculated (or 224.0 N m^{-1} without consideration for sheet thickness). The strain along the zigzag direction results in a stiffening behavior, with an increase of the tangent modulus to 888.4 GPa (284.3 N m^{-1}), or 27% increase over the small-deformation modulus. The mechanistic reason for this increase is that the acetylenic groups align towards the applied strain, resulting in higher sustained stress and strain. An ultimate stress of 107.5 GPa and strain of 0.1324 is determined at failure, which is characterized by multiple fracture sites.

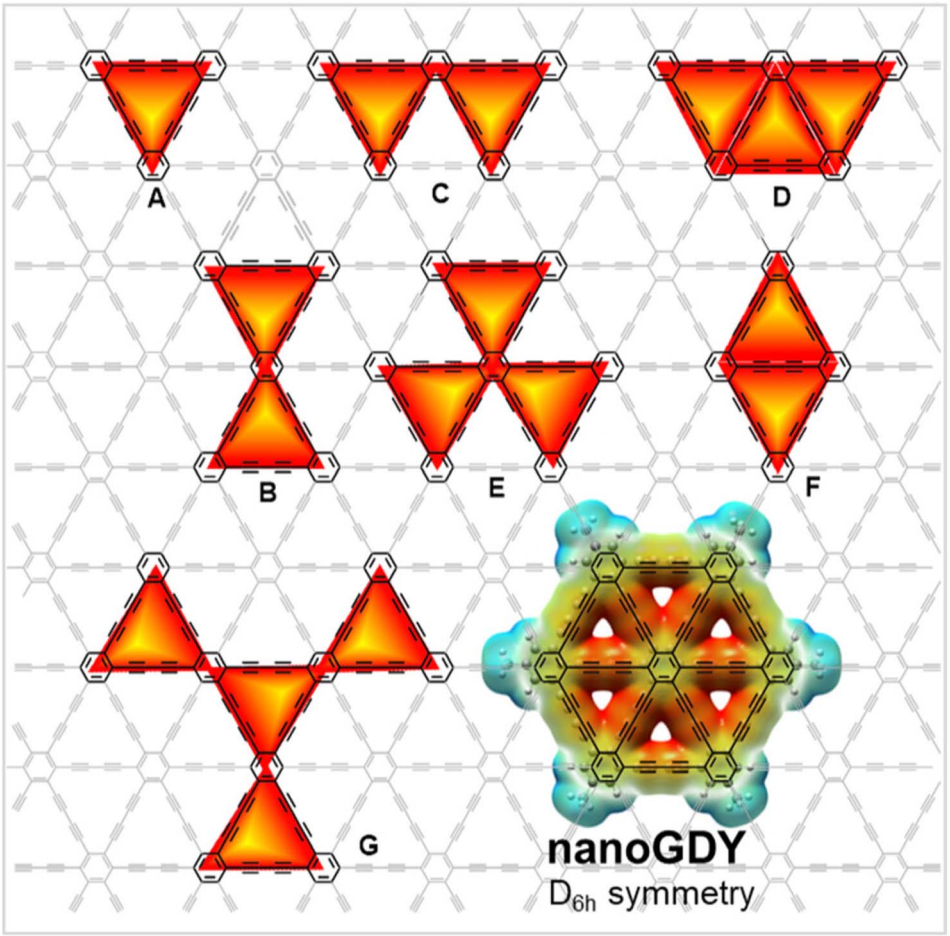

Fig. 11 Structural representations of some nanoGDYs: dehydrobenzo [18] annulene (A), "bowtie" bis(annulene) (B), "boomerang" [18] DBA (C), "half-wheel" annulene (D), trefoil (E), "diamond" substructure (F), GDY substructure (G), and wheel-shaped nanoGDY. Reproduced with permission from Hu *et al.*[111] Copyright 2023, ACS Publications.

fracture stress of a GY network varied. In addition, these 2D materials exhibited anisotropy in their mechanical behavior.

Molecular dynamics simulations were used to compare the mechanical properties of GY-like networks, whose C6 hexagonal rings are connected by chains containing n acetylenic groups (n = 1–5; $n = 1$ for GY and $n = 2$ for GDY).[110] The Young's modulus steadily decreased with an increase in n. However, the fracture strains and ultimate stresses of diverse networks were largely dependent on the type of the applied load, *i.e.*, armchair- or zigzag-like; this finding was attributed[110] to the particular bond elongation and atomic stress distribution among various conformations of acetylenic groups.

Typically, ideal Gra/Gras have been described as long 2D networks without edges and basal plane variations.

However, edges are always present in prepared samples of these materials, and these structural imperfections influence the behaviors and chemical responses of the GYs and GDYs. This aspect must be considered.

2.3. Synthesis of GDY

To harness the application potential of GY-based products, GYs must be readily available in large quantities. Novel synthesis techniques devised in recent decades, such as metal-catalyzed cross-coupling processes, alkyne metathesis, and templated synthesis, have significantly increased the availability of unique molecular (*e.g.*, cyclocarbons) and regular polymeric (*e.g.*, GYs and GDYs) carbon allotropes. Various monomeric and oligomeric substructures of GYs and GDYs have been prepared, as depicted in Fig. 11.[111]

Dehydrotribenzo[12]annulenes, dehydrotribenzo[18]annulenes, and perethynylated expanded radialenes are sections or fragmental model systems of GY and GDY (Fig. 4). These compounds are used as targets in theoretical modeling to further learn about their aromaticity and spectroscopic and electronic properties.[112] Photochromic, highly spin-magnetic, liquid-crystalline, and two-photon-absorption-exhibiting materials can be synthesized from dehydrobenzo[n]annulenes (DBAs). Additionally, they exhibit a high EC upon doping. The specifics of the syntheses of such GY entities have been described.[113] Li *et al.* discovered an *in situ* cross-coupling reaction on a Cu foil that facilitated the fabrication of large-area ordered films of GDY from HEB, enabling a high-yield, direct synthesis of GDY.[41] In the fabrication of the GDY film, the Cu foil functioned as a substrate and as a catalyst for the cross-

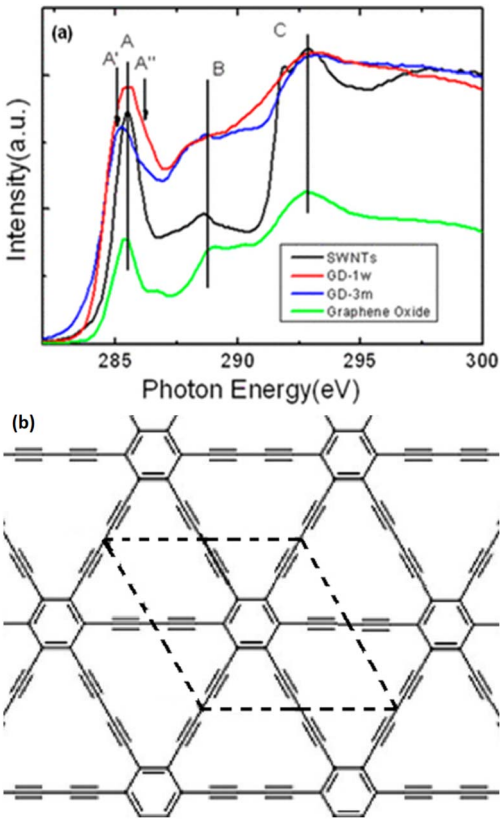

Fig. 12 (a) Comparison of C K-edge X-ray absorption near edge structure spectra of single-walled nanotubes (SWNTs), Gra oxide, and GDY exposed to air for 1 week (GD-1w) and 3 months (GD-3m) and (b) Illustration of the GDY structure. Reproduced with permission from Zhong *et al.*[114] Copyright 2013, American Chemical Society.

coupling reaction, providing a broad, flat area for directional polymerization. Consequently, the formation of a diyne-polymer by polymerization on the flat Cu surface was favored.[41] The as-prepared GDY films were uniform and composed of GDY multilayers. The GDY films exhibited an exceptional semiconducting behavior, as evidenced by their high EC of 2.516×10^4 S m^{-1},[41,74] which is comparable to that of Si. To further research and apply GDY, its electrical structure must be analyzed. X-ray absorption spectroscopy and scanning transmission X-ray microscopy have been used to examine the electrical structure of the GDY exposed to air (Fig. 12).[114]

In the carbon ring structure, Features A, B, and C were attributed to the π* excitation of aromatic carbon–carbon bonds, σ* excitation of carbon–carbon bonds, and interlayer states or transitions to sp^3-hybridized states due to the presence of oxygenated functional groups (*e.g.*, carboxylate), respectively. The introduction of a new feature (Feature A^{II}) with a higher energy than Feature A led to a more significant expansion of Feature A of the GDY exposed for 1 week than of Feature A of SWNTs and G oxide. Feature A, with an energy of ~285.5 eV, was attributed to the π* excitation of unsaturated carbon–carbon bonds (refer to double bonds, triple bonds, or a combination of both) in the carbon ring structure, whereas Feature A^{II} was ascribed to the π* excitation of carbon–carbon triple bonds. These characteristics substantiate the presence of carbon–carbon triple bonds in GDY. The π* and σ* excitations, represented by Features A and C in Fig. 13a, respectively, contributed to the C spectrum and six-membered carbon ring. After 3 months of exposure to air, the carbon–carbon triple bonds at the defect locations in GDY transformed into double bonds. Oxidation occurred throughout the aged GDY, whereas nitrogen contamination occurred primarily on its surface. Experimental investigations have indicated the presence of oxygen and nitrogen functional groups. The triple bond opening caused changes in the bond length, thereby buckling the aged GDY. High-temperature annealing (*e.g.*, 800 °C) may remove a majority of functional groups from the aged GDY.[114] Nearly ten years after the theoretical prediction of GDNTs, arrays of GDNTs were fabricated using an anodic aluminum oxide template, catalyzed by a copper foil (Fig. 13).[45]

After annealing, the wall thickness of the GDNTs decreased from ~40 nm to ~15 nm, and the surface of the as-grown nanotubes became smoother. The GDNTs exhibited high-performance field-emission properties; moreover, the morphology-dependent field-emission properties of the GDNT arrays differed from those of other materials.[45] The annealed GDNTs had low turn-on (E_{to}) and threshold fields (E_{thr}) of 4.20 and 8.83 V mm^{-1}, respectively. In addition, the GDNTs were more stable and had a lower work function than CNTs. ZnO nanorod arrays on a silicon slice were used as the substrate in a vapor–liquid–solid (VLS) growth process to form a unique aggregate structure of GDNWs with a high-quality, defect-free surface. The resulting GDNWs were excellent semiconductors with an EC of 1.9×10^3 S m^{-1} and a mobility of 7.1×10^2 cm^2 V^{-1} s^{-1}. Therefore, GDNWs are potentially useful materials for the electronics and photonics industries.[42] The development of supramolecular analogs by replacing some carbon–carbon covalent linkages in the network with noncovalent bonds would be a novel approach in GY chemistry.[115] Numerous potentially beneficial GDY-based compounds can be synthesized by the effective doping of GDY. For instance, a stable structure with altered BGs was formed by isoelectronic doping of GDY with B and N.[95] After hydrothermal processes, the diacetylenic linkage in GDY partially changed into a 2D π-conjugated structure, which is conducive to electronic transmission, rendering the doped GDY suitable as an electron-transport material in photodegradation processes. Therefore, GDY has been applied to enhance the photocatalytic performance of TiO_2.[44] It is challenging to comprehend the charge-transfer mechanism at the TiO_2–GDY interface because of the convoluted phases and features of the loaded P25 samples. The chemical compositions and electronic characteristics of TiO_2–GDY and TiO_2–Gra composites with various TiO_2 facets were calculated by Wang *et al.*[44] using first-principles density functional theory (DFT) calculations. They discovered that the TiO_2(001)–GDY composite performed better than pure TiO_2(001) or TiO_2(001)–Gra composite in terms of electronic structure, charge separation, and oxidation ability. Hence, the TiO_2(001)–GDY composite could be a highly efficient photocatalyst. In the photocatalytic methylene blue degradation reaction, the rate constant upon using the TiO_2(001)–GDY composite was 1.63

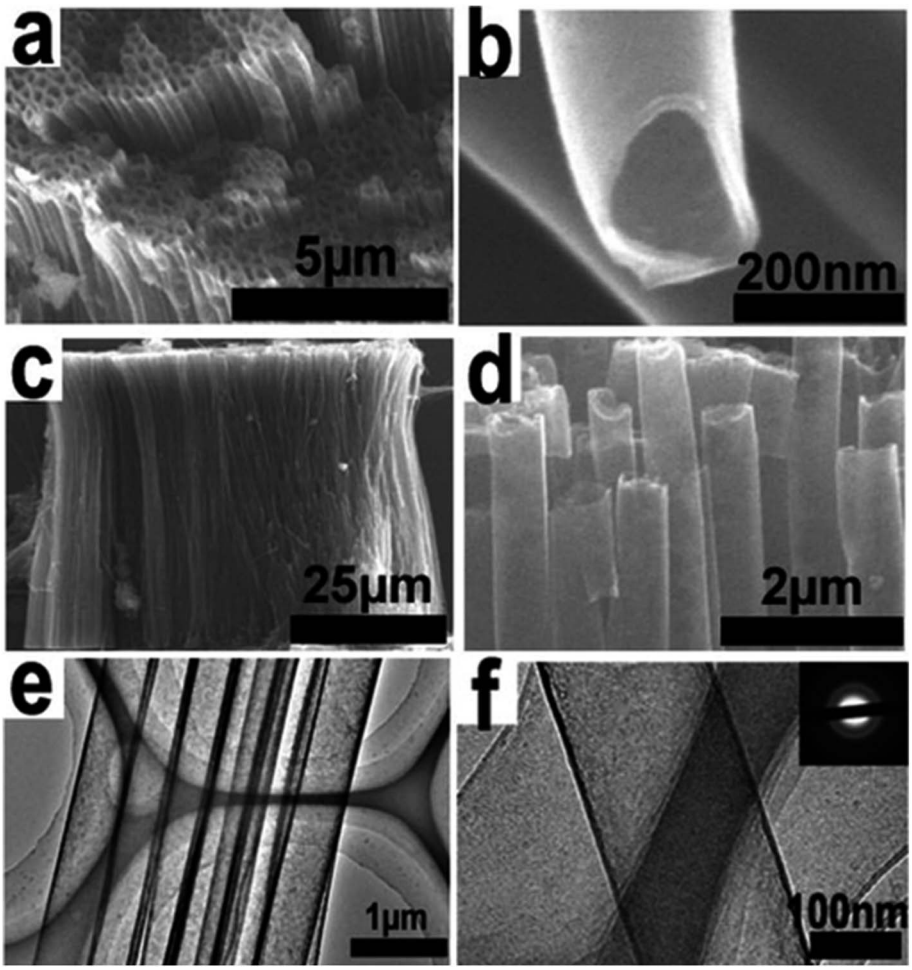

Fig. 13 The SEM and TEM images of GDNTs after being annealed: (a) top view of a GDNT array, (b) top view of GDNTs under higher magnification, (c) side view image of a large area of a GDNT array, (d) side view image of a GDNT array under higher magnification, (e) low-magnification TEM images of a GDNT bundle, and (f) highmagnification TEM images of GDNTs. The inset is the corresponding SAED patterns. Reproduced with permission from Li *et al.*[45] Copyright 2011, American Chemical Society.

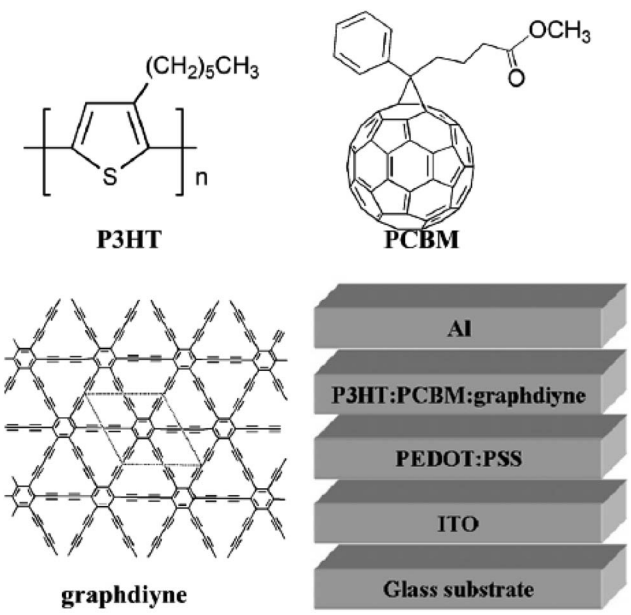

Fig. 14 Chemical structures of P3HT, PCBM, and GDY and the structure of a GDY-containing photovoltaic device. Reproduced with permission from Du *et al.*[116] Copyright 2011, Elsevier Science Ltd.

and 1.27 times higher than those upon employing pure TiO_2(001) and TiO_2(001)–Gra composite, respectively. Thus, GDY could compete with other 2D carbon materials in photocatalytic and photovoltaic applications. Owing to the strong ability of GDY to transport charges and induce effective percolation pathways in the active layer, doping with GDY can increase the short circuit current (J_{sc}) and power conversion efficiency (PCE) of P3HT/PCBM solar cells, as depicted in Fig. 14.[116] The addition of 2.5 wt% GDY increased the J_{sc} of the device by 2.4 mA cm^{-2}, resulting in a peak PCE of 3.53%, 56% greater than that of the equivalent device fabricated without GDY.

2.3.1. Bottom-up 1D and 2D GDY synthesis using ultrahigh vacuum (UHV) settings. Ullmann-type covalent coupling processes rely on thermally accelerated aryl dehalogenation followed by the synthesis of C–C bonds, yielding corrosive and dangerous halogens as by-products.[117–119] In contrast, only hydrogen is produced as the by-product during the homocoupling of acetylenes using the Glaser method. When a logical precursor design is implemented, a wide range of all-carbon 2D materials can be obtained, that is, atomic arrangements with

clearly defined bond sequences and pores that are highly tunable in size and shape. The variations in the coupling mechanism under solution-based reaction conditions have been highlighted in a detailed study on single-crystal metal-surface-assisted synthesis of nanoarchitectures from terminal alkynes in UHV.[120,121]

In 2012, Barth, Klappenberger, and Ruben[122] deposited compounds 1 and 2 onto a Ag (111) surface and observed on-surface-synthesized GDY-based structures by scanning tunneling microscopy (STM) for the first time. Following annealing at 400 K, the homocoupling of the molecules produced 2D irregular open-porous networks with locally ordered domains and honeycomb motifs as the repeating units. They reported the formation of an organometallic dimer after the pristine organic layers formed by 1,3,5-triethynyl-benzene were subjected to a reduced thermal treatment at 300 K, which facilitated an extremely selective dimerization. However, after further thermal activation, intense side reactions interfered with the dimerization, and no long-range order network was observed. Additionally, when alkyne-formed oligomers containing diacetylenic linkages were used as presynthesized monomers on Ag (111), irregular oligomerization occurred.[121] The analysis of the reaction products inferred the formation of 2D conjugated irregular, open-porous networks, comparable to those formed by 1,3,5-triethynyl-benzene. Similarly, a hydrocarbon scaffold with different connecting patterns between up to five molecules was observed when the linear ditopic terphenylene derivate was deposited onto Ag (111).[121]

At nearly the same time (in 2013), Fuchs *et al.*[124] used organic layers formed by diethynyl1,terphenyl with alkane side chains on Au (111). The UHV-STM analysis conclusively demonstrated that all the molecules were oligomerized through covalent coupling of the alkyne functionalities. The oligomers could be moved using the STM tip without damaging the linkages; however, several side products were also formed. In addition to the intended product (butadiyne), other coupling patterns formed *via* the covalent coupling of up to four monomers. Such patterns underwent various side reactions such as *E*/*Z* hydrogenation, insertion reactions, and alkyne trimerization, affording bifurcation points with benzene core structures inside the as-formed 2D networks (VI).

Wang *et al.* successfully controlled the reaction system of 1,1′-biphenyl-4-bromo-4′-ethynyl (BPBE) on Ag (111), which could undergo three coupling reactions, namely, Glaser, Ullman, and Sonogashira and coupling. Different kinetic approaches can result in the formation of either Gra or GDY nanowires. Through the hierarchical activation of Glaser coupling, which has the lowest energy barrier, and the Ullman

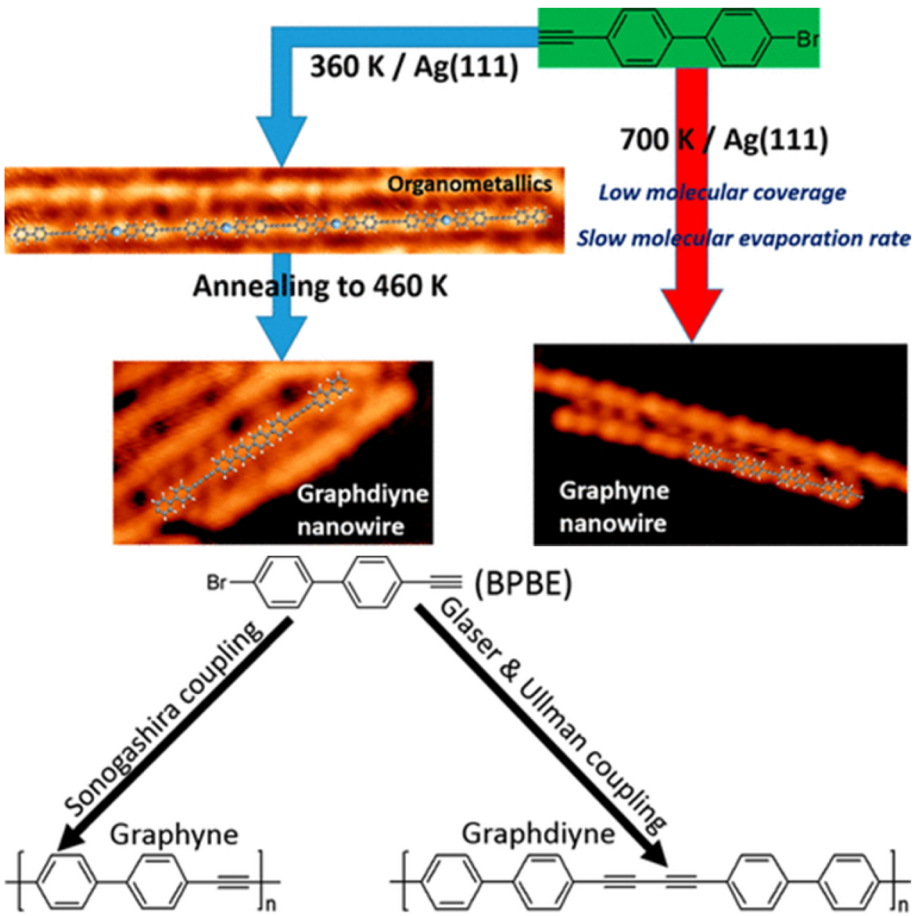

Fig. 15 (a) Schematic of GY and GDY preparation along with their resultant STM micrographs and (b) potential formation pathways of GDY and GY nanowires from BPBE. Reproduced with permission from Wang *et al.*[123] Copyright 2018, ACS Publications.

coupling of BPBE, GDNWs were fabricated in the most energetically favorable manner. Moreover, the formation of GY nanowires was attributed to the high selectivity of the high-energy-barrier Sonogashira coupling, whose essential kinetic parameters are high surface temperature, low molecular coverage, and low precursor evaporation rate, as deduced from a series of control experiments (Fig. 15).[123]

Several strategies, such as geometrical shielding of the butadiene linkage and templating on vicinal surfaces, have been devised to address the challenges associated with fabricating regular GDY networks and to boost control over on-surface activities. Fuchs *et al.*[124] prepared 1,4-diethynyl-2,5-dihexylbenzene 6 by adding *ortho*-substituents near the alkyne functionality. The statistical analysis of the as-formed products confirmed the preference for linear C–C homocoupling over other covalent coupling schemes when bulky side groups were located near the alkyne functionalities and were combined with the Ag (111) surface. Liu *et al.*[125] established a method to synthesize 1D covalently bounded GDY molecular chains as the major product following the annealing of 2,5-diethynyl-1,4-bis(phenylethynyl)benzene 7. The efficient steric shielding provided by the large phenylethynyl group resulted in a relatively high yield of approximately 70%.

Alternatively, a templating strategy that implements high-index surfaces can yield lengthy polymer chains while suppressing chain branching. Barth, Ruben, and Klappenberger employed the Ag (877) vicinal surface to increase the chemoselectivity for guiding the carbon–carbon coupling reaction toward linear butadiyne scaffolds.[121] The preferred adsorption sites of compound 3 were identified by evaporating compounds onto Ag (877) substrates at 186 K. The aromatic backbones of the molecules were parallel to the step edges, resulting in their preferential adhesion. Even at saturation, regular alignment along the step edge proved advantageous and represented optimal pre-reaction ordering. Wires composed of 1D extended GDYs, with a length of 30 nm, were produced after annealing at 450 K. Finally, *in situ* chain manipulation using lateral STM tip displacement demonstrated the consistency and stability of the newly formed bonds. A preliminary assessment of their electronic characteristics using DFT computations identified GDNWs as 1D semiconductors with a theoretically advantageous, direct electronic band structure.[121]

In another study, silver acetylides, considered the most effective reactants in the transformation of alkynes, could be easily formed when terminal alkynes combined with metal atoms to generate acetylides.[126]

However, organometallic nanostructures have been synthesized on surfaces in only a few studies. When 2,5-diethynyl-1,4-bis(phenylethynyl)benzene 7 was used on Ag (110) and Ag (100), 1D organometallic molecular wires were produced with a yield of approximately 90%, as depicted in Fig. 16.[125] Experimental and theoretical analyses on Ag (111) revealed a lattice-type

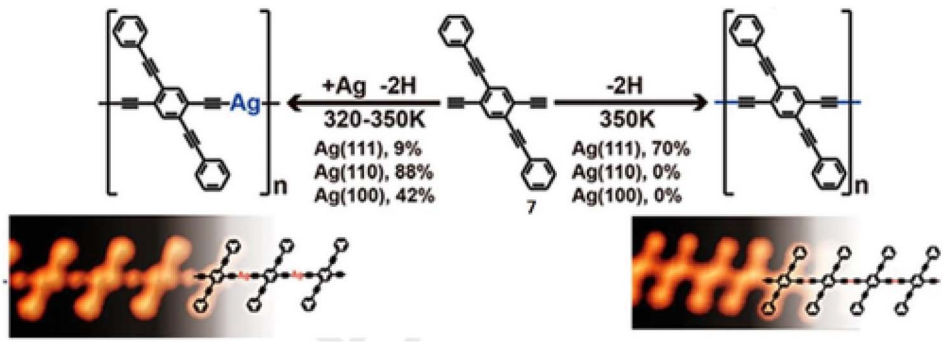

Fig. 16 Different lattice planes of Ag substrates trigger the reaction pathways and main products: homocoupling is dominant on Ag (111), whereas Ag (110) triggers the formation of highly oriented 1D silver acetylide organometallic chains. Reproduced with permission from Liu *et al.*[125] Copyright 2015, American Chemical Society.

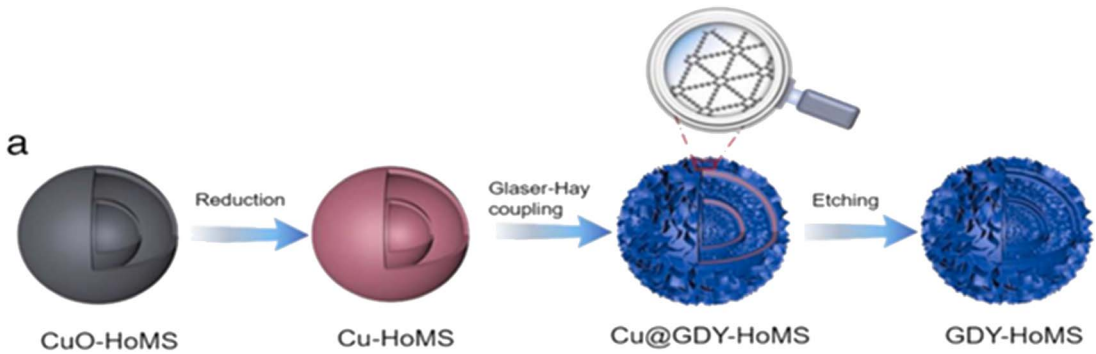

Fig. 17 (a) Schematic of the synthesis process of Cu@GDY–HoMS (HoMS: hollow multishelled structure) and GDY–HoMS. Reproduced with permission from Zhan *et al.*[128] Copyright 2022, Elsevier Science Ltd.

dependence of the terminal alkyne reaction due to the degree of epitaxial matching between the respective periodicities of the produced molecular wires and the underlying substrate lattices.

Controlled production of highly regular, low-dimensional, all-carbon nanoscaffolds can be rendered feasible by the organometallic bonding of molecular precursors with alkynyl functionalities.

Sun *et al.*[127] investigated the dehalogenative homocoupling reactions of various terminal alkynyl bromides on Au (111) surfaces to construct dimer structures, 1D molecular nanowires, and highly regular 2D molecular honeycomb networks of GDY nanostructures. The sequential characteristics of the chemical process were revealed by combining DFT calculations and high-resolution (HR)-STM imaging. In the first step after moderate annealing, large-area C–Au–C organometallic networks were formed. When the annealing temperature was greater than 420 K, 1D molecular wires and a 2D molecular network with acetylenic scaffolds were formed.

Zhan *et al.*[128] prepared Cu–HoMS by first synthesizing CuO–HoMS and then reducing it using a sodium borohydride solution; Cu–HoMS functioned as the skeleton and template for GDY development (Fig. 17). Subsequently, Cu–N composites were developed on the surface of Cu–HoMS in a mixture of acetone, pyridine, and *N*,*N*,*N*′,*N*′-tetramethylethylenediamine (TMEDA), using a catalytic organic base (pyridine and TMEDA), which is a crucial catalyst for the coupling reaction of HEB to form GDY. The porous shell of HoMS enabled the penetration of all minute molecules, following which GDY could grow on both the inner and outer shells of HoMS and on their respective surfaces. Consequently, Cu@GDY–HoMS was produced, which could then be converted into GDY–HoMS by Cu etching using 0.5 M $FeCl_3$.[128]

Hu, He, Chen, and Li[111] have recently proposed the synthesis of wheel-shaped nanoGDY consisting of six DBAs [18] ([18], the smallest macrocyclic unit of GDY). They repeatedly synthesized wheel-shaped nanoGDY *via* sixfold intramolecular Eglinton coupling within hexabutadiyne precursors, which was realized through sixfold Cadiot–Chodkiewicz cross coupling of HEBs[111] (Fig. 18). They established the planar structure of the overall 18π-electron cross-conjugation using X-ray crystallography, resulting in a giant π core containing π-electrons (Fig. 19). This synthesis approach is a significant breakthrough in synthesizing GDYs with desired functionalities and heteroatomic doping.

Corrosive and dangerous halogens are produced as by-products of dehalogenative homocoupling reactions; however, this on-surface transformation offers an alternative method for preparing typical low-dimensional GDY nanostructures. Further novel eco-friendly approaches for GDY-based systems must be strategized for advanced applications through the

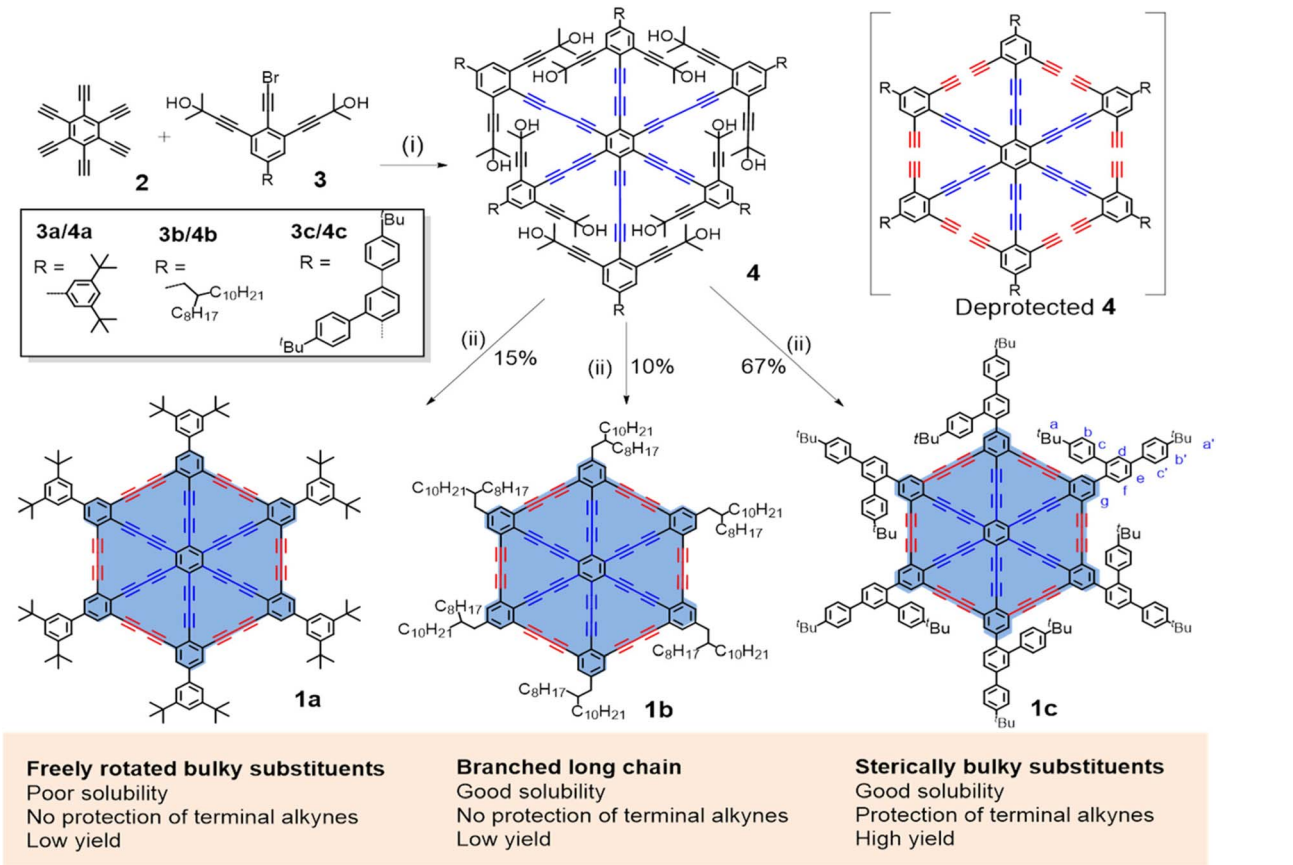

Fig. 18 (a) Synthesis route for nanoGDY. (i) $Pd_2(dba)_3{\cdot}CHCl_3$, CuI, *N*,*N*-diisopropylethylamine, DMF/toluene, rt; (ii) (a) KOH, toluene, 120 °C; (b) CuCl (60 equiv.), and (c) $Cu(OAc)_2{\cdot}H_2O$ (60 equiv.), pyridine, 60 °C. Reproduced with permission from Hu *et al.*[111] Copyright 2023, American Chemical Society.

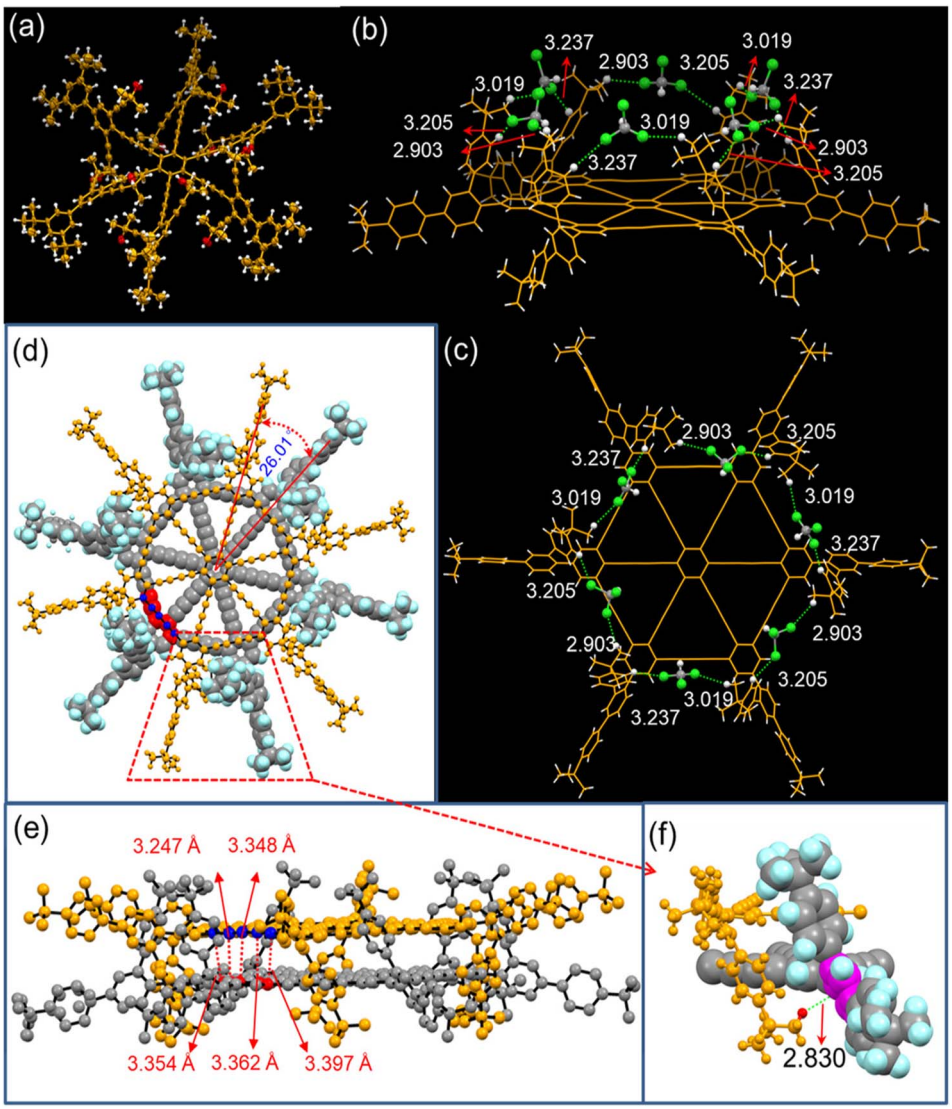

Fig. 19 X-ray crystallographic structures of 4a (a) and 1c (b and c) at 170 K, (b) side view and (c) top view of 1c, with *ortho*-substituted 4-(*tert*-butyl)phenyl groups vertical to the nanoGDY core plane with an included angle of 62.3°; the H···Cl hydrogen bonds formed between H atoms of *tert*-butylphenyl groups in 1c and the Cl atom in the solvent $CHCl_3$ are shown. Top view (d) and side view (e) of dimer 1c with close contacts (purple dashed lines with labeled distance); the carbon atoms in different layers with close contacts are highlighted in red and blue colors. (f) Enlarged view in red trapezoid to show the CH···π interactions. Reproduced with permission from Guilin *et al.*[111] Copyright 2023, American Chemical Society.

generation of nontoxic by-products or the collection and conversion of toxic products into value-added chemicals.

2.3.2. Solution-based synthesis of GDY films on copper foils. The bottom-up method combined with HR-STM molecular imaging in UHV at well-defined metal surfaces allows for the investigation of chemical processes at the single molecular level, providing deep insights into the absorption geometries and chemical states of precursors, intermediates, and products. However, the technological potential of this approach for large-scale GDY production is limited.

Scientists have attempted to synthesize GDY films on Cu foils in solution in the presence of a base by combining the metal catalyst in the UHV system, with the Cu salt acting as the catalyst in solution.

In 2010, Li *et al.* first reported the *in situ* synthesis of GDY on a copper foil using HEB 10 as the starting material for a cross-coupling process.[41]

The precursor (HEB) was reacted *via* a cross-coupling reaction for 72 h at 60 °C in an argon environment as the GDY was grown on a copper foil in a pyridine solution. A graphdiyne film with a large area of ~3.6 cm^2 was grown on the copper foil support, which enabled directional growth of the GDY film because of its substantial flat surface area.

After transferring the film onto a silicon substrate, it was investigated by Raman spectroscopy, atomic force microscopy (AFM), SEM, and TEM. The GDY edge of the copper foil exhibited some curling, indicating the flexibility of the material. The thickness of the GDY film was evaluated by AFM; the film possessed an average thickness of 970 nm and exhibited

a layered architecture. The multilayer film was imaged by high-resolution transmission electron microscopy (HR-TEM). The bright spots in the selected area electron diffraction pattern and the lattice fringes of 4.19 Å suggesting that the film was crystalline.[129]

Raman measurements were performed at several locations on the film, and all the spectra revealed four primary peaks at 1382.2, 1569.5, 1926.2, and 2189.8 cm^{-1}. The homogeneity of the film was determined from these peaks. Based on a theoretical analysis, the peak at 1569.5 cm^{-1} was caused by the –C=C– aromatic stretching mode of the C6 rings, which was comparable to the G band of Gra. Because the sp^2- and sp-hybridized carbon atoms contributed to the peak at 1382.2 cm^{-1}, a new D′ mode was present in the spectrum, differing from that of Gra. The peak at 2189.8 cm^{-1} confirmed the existence of conjugated diyne –C≡C–C≡C– linkages. The peak at 1926.2 cm^{-1} was attributed to monoyne moieties; thus, some remaining triple bonds did not undergo the homocoupling reaction. Further structural quality improvements are necessary to optimize GDY, given that all the modes were significantly wider than those of high-grade Gra.[130]

The electrical characteristics of the films were investigated using a Cu foil and Al films as the bottom and top electrodes, respectively. The EC was 2.5×10^4 S m^{-1}. Even though the results appear promising, further research is required to fully comprehend the nature of this conductivity, including the reasoning behind the nonexistence of Schottky contacts, which are typically present at a metal–semiconductor interface,[131] and the origin of essential charge carriers.

Li *et al.*[132] developed analogous carbon nanofilms using ZnO nanorod arrays as the substrate and Gra powder as the starting material. *In situ* cross-coupling reaction was performed to obtain the precursor powder. Continuous layers of nanofilms were developed on a substrate with a thickness at the nanometer scale (Fig. 20a–c).

The optical microscopy image (Fig. 20b) revealed a large continuous area of greater than 4.8 mm^2, with a highly smooth structure. Nanofilms with a thickness of 22 nm exhibited a weak contrast with the substrate. They contained approximately 30 or more Gra layers (Fig. 20).

Raman spectroscopy was conducted to further characterize the nanofilm. The intensity of the modes associated with monoyne (1930 cm^{-1}) and diyne (2180 cm^{-1}) moieties relative to those attributed to the sp^2-hybridized carbon atoms (1380 cm and 1570 cm^{-1}) was substantially lower than theoretical predictions[20] and lower than that observed in a previous synthesis technique.[41] The ZnO method partially targeted the triple bonds, as evident by the decrease in the intensity of high-energy modes. Furthermore, HR-TEM analyses revealed streaks on the film sample, and the gap between a pair of streaks was approximately 0.365 nm (Fig. 20).

A bottom-gate thin-film transistor (TFT) was fabricated on octadecyltrichlorosilane (OTs)/SiO_2/Si by evaporating Au electrodes directly on the GDY TFT to explore the electrical properties of the prepared nanofilm. More than 100 devices were used for investigating the electrical performance; the average mobility was 30 cm^2 V^{-1} s^{-1}. However, this value is significantly smaller than the theoretical value for an idealized GDY monolayer (200 000 cm^2 V^{-1} s^{-1}).[73] Moreover, similar discrepancies have been reported for the theoretical predictions of *G* and non-epitaxial films.

In 2015, Zhou *et al.*[133] implemented a modified Glaser–Hay coupling technique and synthesized Gra nanowalls for the first time (Fig. 21a). The interconnected 2D nanosheets that stood vertically on the substrate were referred to as nanowalls. Acetone, TMEDA, and pyridine were used in an adjusted ratio with a copper plate instead of a copper salt to conduct the Glaser–Hay coupling reaction. These ions served as catalysts in the reaction because metallic copper rapidly oxidizes to copper ions in the presence of a base. The modification enhanced several aspects of the original procedure: the coupling reaction

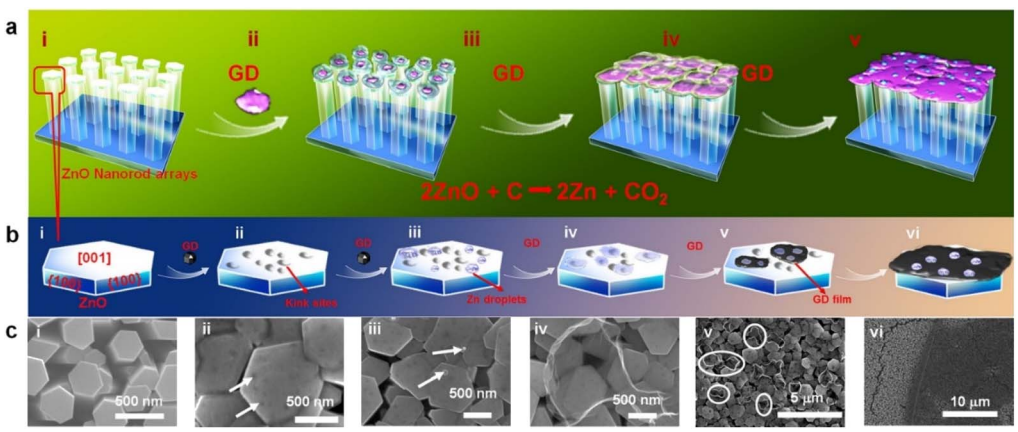

Fig. 20 (a) Schematic of growth of a GDY film, combining a reduction with a self-catalyzed and saturated VLS model. (b) Schematic of growth of a GDY film, combining a reduction with a self-catalyzed and saturated VLS model on the top surface of a single ZnO nanorod (NR). (c) SEM images corresponding to the schematic in (b) of (i) ZnO NRs with smooth top surfaces and thin GDY films; (ii) rough surface and kink sites (marked with arrows) produced by ZnO reduced atop the ZnO NRs; (iii) ZnO nanoparticles, which originated from reoxidized Zn droplets, scattered in the GDY thin films; (iv) a typical droplet-like transparent GDY thin film; (v) many small GDY thin films, produced by a few Zn droplets, connected by two, three, or more fragments of a smaller GDY film; the morphologies of the small GDY films are similar to those of the droplets; (vi) continuous large-area GDY thin films. Reproduced with permission from Qian *et al.*[132] Copyright 2015, Springer Nature.

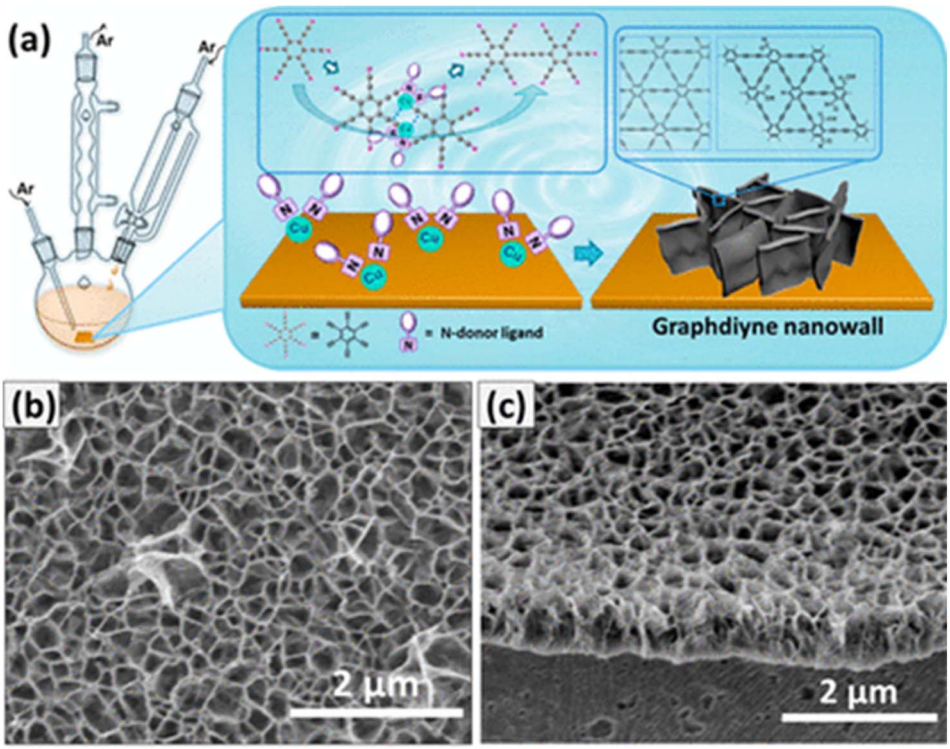

Fig. 21 (a) Schematic of the experimental setup. (b) Cross-sectional view of the SEM image of GDY nanowalls on the Cu substrate. (c) AFM image of the exfoliated sample on the Si/SiO_2 substrate. The height profile is taken along the white line, representing a 15.5 nm thick film. Reproduced with permission from Zhou *et al.*[133] Copyright 2015, American Chemical Society.

was conducted in acetone, which is not an alkaline solution. Because the reagents were more soluble, the yield increased. Additionally, the mild acidity of the solution favored the stability of precursor 6 (HEB); it was more stable than that in the original pyridine solution. Furthermore, Gra nanowalls could be formed consistently by adjusting the amount of N-ligand.

The SEM image revealed a continuous matrix of vertically built nanowalls with significant voids (Fig. 21b). The cross section indicated that the nanowalls were highly homogeneous, with a height of ~100 nm throughout the surface. After evaluating a mechanically exfoliated GYD film transferred onto a silicon surface, the thickness (15.5 nm) of the nanowall films was measured by AFM. Several nanowall films exhibited a high crystallinity, as determined by HR-TEM. In accordance with the theoretical values, the lattice fringe was measured at 0.466 nm. Another crystal shape suggested the presence of curved GDY sheets in the film, whose lattice parameter was larger (0.365 nm) than that of Gra. The value of GDY spacing between carbon layers (0.365 nm) was slightly greater than that of Gra (0.142 nm), suggesting that it is a more delocalized system.[133]

The four prominent Raman peaks at 1383.7, 1568.7, 1939.8, and 2181.1 cm^{-1}, which were commonly observed in the spectra of GDY, were visible in the Raman spectra of nanowalls. The triple-bond-related modes were significantly more noticeable herein, demonstrating the better structural quality of GDY due to the nanowalls. The typical emission density *versus* applied electric

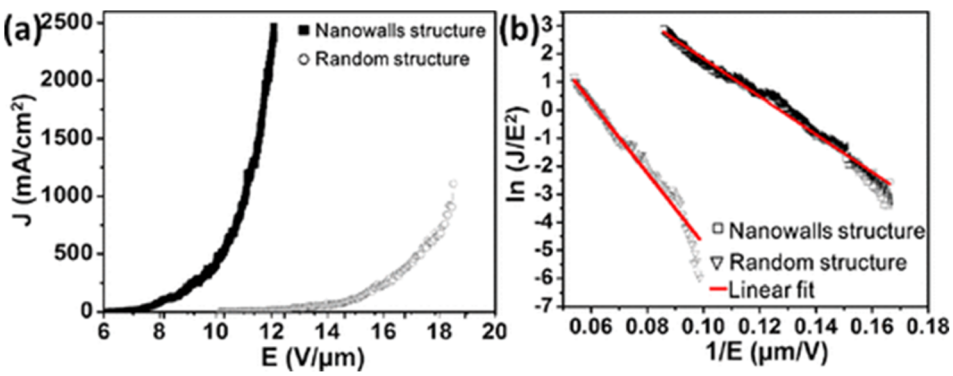

Fig. 22 (a) Typical plots of electron-emission current density (J) as a function of applied electric field (E). (b) Corresponding F–N plots and linear fitting. Reproduced with permission from Zhou *et al.*[133] Copyright 2015, American Chemical Society.

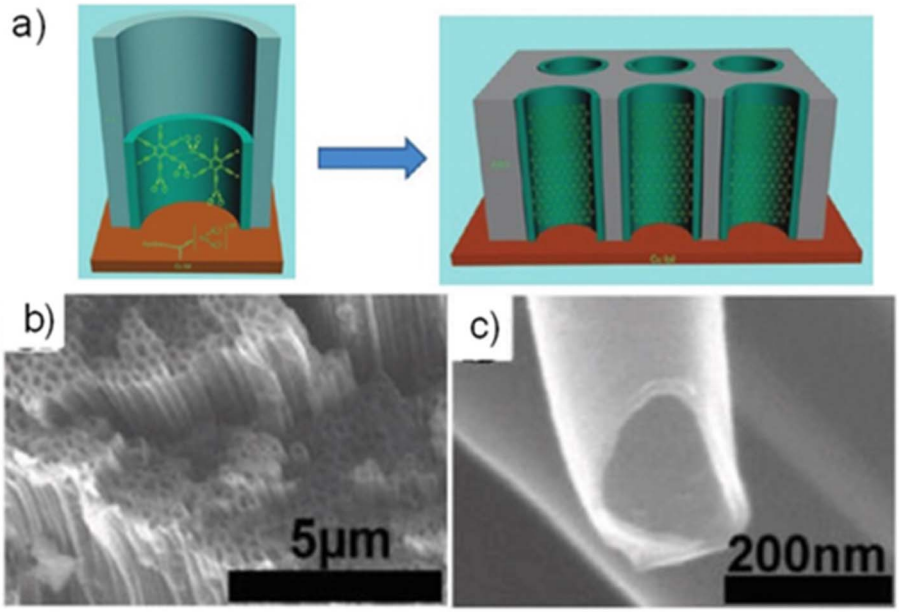

Fig. 23 (a) Process and proposed mechanism to synthesize GDNT arrays. (b and c) SEM images of GDNTs after annealing. Reproduced with permission from Li *et al.*[45] Copyright 2011, American Chemical Society.

field (*J*–*E*) plot indicated the field-emission performance of the GDY nanowalls: the E_{to} and E_{thr} were approximately 6.6 and 10.7 V μm^{-1}, respectively (Fig. 22a). Graphdiyne has a lower carrier mobility than *G*; hence, its E_{to} and E_{thr} values were slightly larger than those of a vertical sheet of G. The GDY nanowalls generally exhibited good field-emission properties, consistent with the Fowler–Nordheim theory (Fig. 22b), which attributed the electron emission from nanowalls to tunneling. This observation is valid, even though the E_{to} of GDY is considered to be low among the field emissions of commonly used devices.[133]

The implementation of a VLS growth process facilitates the synthesis of highly ordered, high-crystallinity, and almost defect-free nanomaterials. In addition, it affords a tractable approach to nanoparticle synthesis. This approach has been paired with techniques for coating surfaces with catalytic metals, such as Au, Fe, and Ni.

In the research on GDY nanostructures for nanoelectronics, GDNTs, which are a distinct 1D version of GDY, have been prepared. Regarding the aspect ratio, nanotubes and nanowires are similar tube-shaped structures with the size at the nanometer scale. However, unlike wires, which are solid structures, tubes are hollow and can consist of one or more walls. Li *et al.*[45] attempted the synthesis of GDY-based carbon tubes similar to Gra-CNTs for the first time, using an anodic aluminum oxide template, one side of which was glued to a copper foil (Fig. 23a–c).

3. Applications of GDY in desalination and wastewater remediation

Wastewater contaminants such as heavy toxic dyes, pesticides, and radioactive nuclides and the high toxicity and long-term retention of metallic ions in surface water environments pose threats to ecosystem stability and the health of living organisms, including human beings. Widely used approaches must comply with the aspects of sustainability and energy use. It is imperative to determine a suitable and efficient method for excluding these contaminants because the discharge criteria for contaminants/pollutants in water are quite strict. The following subsections discuss the applications of GDY in water remediation, as reported in recent decades.

3.1. GDY for desalination

Despite its abundance on Earth, most water is saline. Desalination is one of the most effective methods to provide fresh, potable water while facilitating water reuse. Desalination is defined as a procedure of removing salt ions from clean water and is advocated as a practical solution to the problem of water shortage. The function of membranes is pivotal in all desalination techniques.

Traditional water treatment methods have drawbacks such as high energy usage, poor separation performance, and rigid requirements for water temperature. These issues have been effectively resolved by the membrane separation technology. Owing to its benefits, the membrane separation technique is a crucial novel technology for addressing the pressing problems associated with the resources, environment, and energy, among others. These advantages include obtaining a high separation coefficient, preventing phase changes in the material during the separation process, and executing the procedure at room temperature. Numerous membrane-based water and wastewater systems have been introduced into the market, *e.g.*, traditional pressure-driven brackish and saltwater reverse osmosis (RO), osmotically driven forward osmosis, microfiltration, nanofiltration (NF), and ultrafiltration.[134]

Reverse osmosis is one of the most energy-efficient and environmentally efficient desalination technologies available to date, outperforming techniques such as thermal desalination.[3,4,134] Because of the slow water flow through typical RO membranes and the technical challenges related to tunable pore sizes, desalination is not widely used to address freshwater shortage. Consequently, desalination remains expensive and inefficient.

The abovementioned problem was addressed by using innovative porous nanomaterials as RO membranes to improve the desalination performance, by which water could be quickly transported across the distinct nanopores. The pore widths of the membranes, along with those of the nanotube or nanosheet membranes, must be properly regulated. The opening edges of nanosheets or nanotubes must be chemically modified with particular functional groups to completely segregate all ions from seawater using these nanomaterials. Therefore, it is critical to identify novel membrane materials with inherent, clearly defined nanopores of appropriate size for highly efficient desalination. Owing to the unique qualities of sp^2-hybridized carbon bonds, carbon-based nanomaterials possess excellent chemical and physical properties at the nanoscale. Regarding environmental challenges, carbon-based nanomaterials exhibit good single-molecule and bulk features, such as the high surface area, porous architecture, high EC, good antifouling character, the possession of the adsorption potential of bulk nanomaterials, and so on. Recent investigations have demonstrated that GY membranes have a high mechanical strength and can resist deformations due to the installation process or other external limitations and withstand water pressure.

Membrane production has advanced relatively slowly. Therefore, assessing and tuning the molecular properties of a membrane are desirable to attain an increased water flux and water permeability. Hence, it is preferable to conduct computer simulations of the structural aspects before producing membranes. Molecular dynamics (MD) simulation is an effective computational technique that uses a force field to solve the Newton's equations of motion to study the interactions between particles. Additionally, the effects of bonded or intramolecular interactions and intermolecular or nonbonded interactions on the behavior of molecules and ions in the system can be analyzed.

With the aforementioned benefits as a driving force, Banan Baghbani *et al.*[135] conducted MD simulations to examine the capability of a pure GDY membrane in saltwater desalination. The membrane under study had inherent pores but lacked a chemically functionalized surface. The pressure difference drove the system, which consisted of the pure GDY membrane, water molecules, and ions. High water flux and high salt rejection are the two complex aspects in membrane-based desalination processes; hence, the water density, salt rejection, and radial distribution function were evaluated. The results showed that at pressures below 150 MPa, water molecules could not travel through the GDY membrane. At higher pressures, the water molecules could move across the membrane, with a substantial water flux.

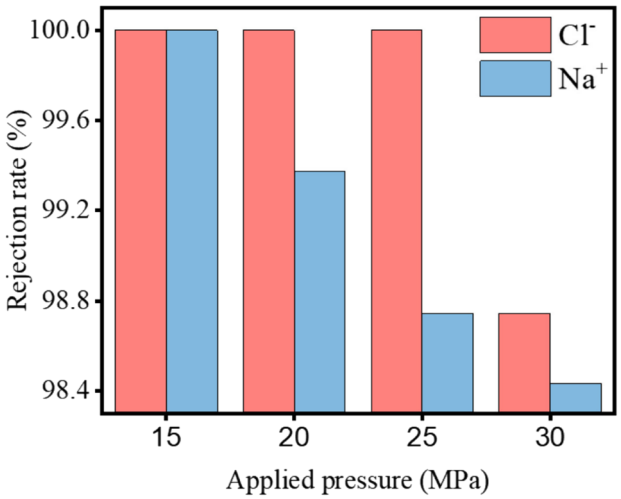

Fig. 24 Seawater desalination properties of GDY. Ion rejection efficiencies of GDY with respect to applied external pressure in the range 10–25 MPa. Cumulative volume of water passed at different hydrostatic pressures. Reproduced with permission from Xu *et al.*[136] Copyright 2023, Elsevier Science Ltd.

However, the ions could not travel through the membrane even at high pressures. The capability of GDY for the purification process can be represented by the potential of the mean force (PMF) graphs. The PMF increased when ions or water molecules were near GDY. Additionally, the Na^+ and Cl^+ ion PMF peaks were higher than those of the water molecules, indicating that the GDY membrane presented a higher energy barrier for their transit. This could be ascribed to the strong interactions between the ions and GDY atoms. Therefore, pure GDY nanosheets offer excellent potential for separating salt ions, particularly at high pressures.

Xu *et al.*[136] performed a complete analysis of the desalination process using the DFT and MD to define the electron-level mechanism of sodium-ion transport in periodic, self-cleaning nanosized pores. The as-produced GDY, which exhibited periodic pores, electrical characteristics, and a stable structure, was among the most promising desalination membranes. Compared to other 2D materials, GDY membranes required less pressure and exhibited a greater salt rejection rate of 100% (Fig. 24). The transition-state energy of Na^+ in a GDY membrane was sufficient (0.03 eV) owing to the charge transfer between the carbon atoms in the periodic pores and sodium ions in the p_z orbitals, endowing the GDY membrane with a metallic nature while preventing the filtration and aggregation of Na^+. Therefore, the periodic conductive network could facilitate the reuse of RO membranes under the influence of an electric field, thereby enhancing their serviceable life, unlike traditional polymeric thin films. Thus, the authors introduced a novel method for designing and monitoring emerging desalination membranes, which is the final stage in addressing the issue of introducing periodic nanosized pores in 2D carbon materials.

Majidi *et al.* examined the ion rejection of a membrane to examine the separation capabilities of GDY. The hydrated forms of NO_3^- and Na^+ had diameters of approximately 7.0 and 6.4 Å,

respectively, larger than the pores in the Gra nanosheet. The results of their models demonstrated that the ion rejection efficiency of the GDY membrane was 100%, even at an elevated pressure of 500 MPa. Because no hydrophilic atoms or bonding sites were present in the structure of the GDY membrane to facilitate ion dehydration, unlike the case of amine-functionalized γ-GY-1, the GDY membrane had a stronger ability to reject ions.[2] Moreover, the effective pore size of GDY was less than the effective diameter of the ions.

Thus, GDY and GDY-based materials are excellent candidates for wastewater treatment *via* membrane-based desalination: they perform better than commercially available desalination membrane systems. However, membrane production has advanced slowly. Therefore, the molecular characteristics of a membrane should be evaluated and designed to optimize water flux and permeability. Hence, a study of structural features *via* computer modeling is preferred before membrane fabrication. In an MD simulation, a force field is used to solve the Newton's equations of motion to examine the interactions between particles. Additionally, the effects of bound or intramolecular contacts on the behavior of molecules and ions in the system and the effects of non-bonded or intermolecular interactions can be investigated.

3.2. GDY for oil–water separation

Oil spills into water bodies lead to significant water pollution, adversely affecting human health and the surroundings. Water pollution caused by oil or leakage can be addressed using several techniques, including filtration, use of chemical dispersants, and simple mechanical assortment. However, these methods either consume much energy or have a low efficiency. The use of appropriate adsorbents with a high selectivity, adequate recyclability, and good adsorption capability is a highly cost-effective method for oil–water separation. In this regard, adsorbents with sponge- or foam-like structures facilitate the selective accumulation of oil. The generation of microstructures on porous substrates *via* an effective means would facilitate the synthesis of superhydrophobic adsorbents with the desired wettability.

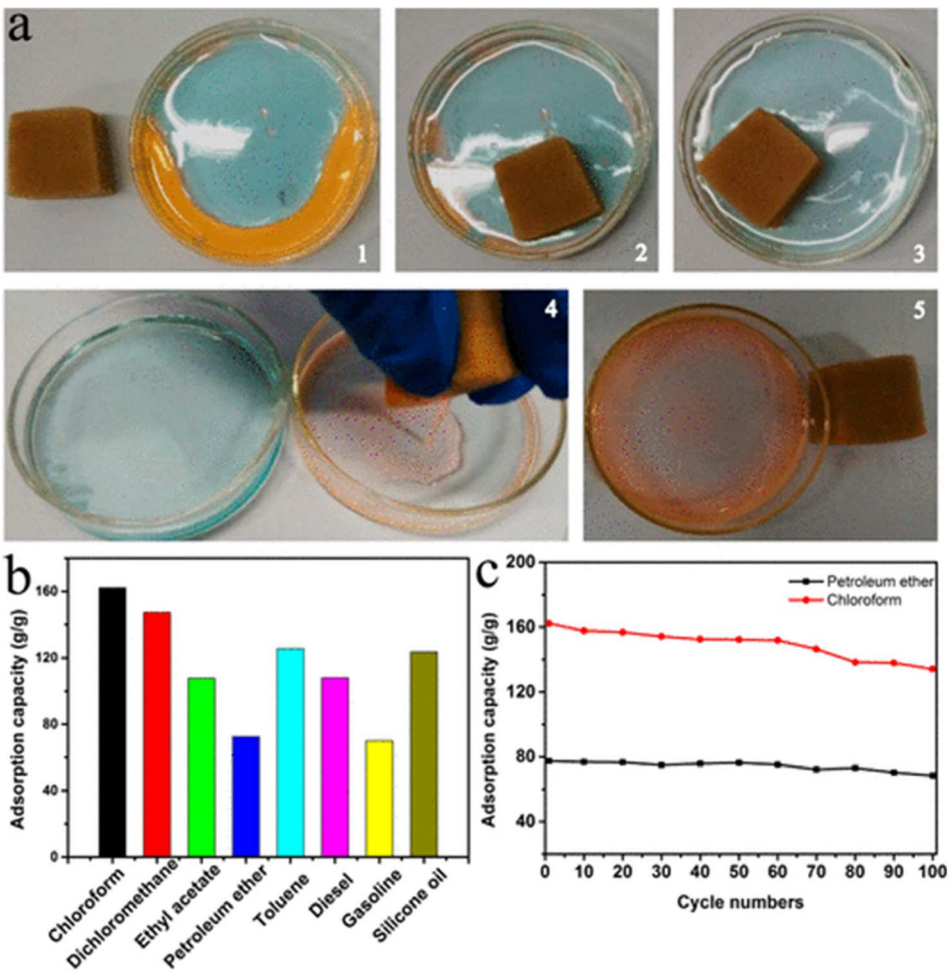

Fig. 25 Performance of GDYMS as an oil accumulation material. (a) Photographs of GDYMS-15 recovering an organic solvent from an oil–water mixture. (b) Adsorption capacities of GDYMS-15 toward various organic solvents and oils. (c) Adsorption recyclability of GDYMS-15 toward petroleum ether and $CHCl_3$. Reproduced with permission from Li *et al.*[137] Copyright 2019, American Chemical Society.

Table 3 A summative comparison of GY/GDY-based oil–water separation membrane efficiencies as per the literature

Membrane	Oil–water separation efficiency (%)	Water contact angle (°)		Citation
		Air	Oil	
PDMS–GDY-grown Cu foam	>98	160.1	171.0	138
GDYMS-15	>97	132	—	137

Li *et al.*[137] incorporated GDY into the backbone of a melamine sponge *via* an *in situ* Glaser–Hay coupling reaction. Owing to its hydrophobic nature, the GDY-coated melamine sponge (GDYMS) exhibited excellent adsorption of oil and organic solvents, amounting to 160 times its original weight (Fig. 25a). In addition, because the composite sponge remained highly stable in corrosive solvents, it could be used for extracting organic solvents such as chloroform, dichloromethane, ethyl acetate, petroleum ether, toluene, diesel, gasoline, and silicon oil, as depicted in Fig. 25b. The material could be recycled for up to 100 cycles without any significant loss in its adsorption capacity, as shown in Fig. 25c. Furthermore, the contact angle of 132° and recyclability of 100 cycles increased the effectiveness of the material. Similarly, Gao *et al.*[138] used a copper foam as a substrate for preparing nanoGDY *via* an *in situ* Glaser–Hay coupling reaction. A bilayered micro–nanostructure was constructed, which imparted roughness to the surface. The as-obtained material was coated with poly(dimethylsiloxane) (PDMS), forming a superhydrophobic foam with a contact angle of 171.0° in oil. Moreover, the foam was abrasion-resistant.

When the water contact angle is ≤90°, ≥90°, and ≥150°, the solid surface is hydrophilic, hydrophobic, and superhydrophobic, respectively. Higher contact angles are desirable, which correspond to superhydrophobic surfaces for GDY-based materials (Table 3) aimed at oil–water separation.[138] The contact angle and separation efficiency are related, and a greater hydrophobicity and lipophilicity are associated with an improved oil–water separation performance of the GY/GDY oil–water separation membranes.

Although GDY and GDY-based materials have been established as efficient materials for oil–water separation, there are limited reports on the same. The practical adoption of GDY-based membranes/systems merit further exploration, considering their exceptional results as per the limited available literature.

3.3. GDY for heavy-metal removal

Because of their toxicity and potential carcinogenicity in humans, heavy-metal pollution in nature—especially in aquatic habitats such as industrial or agricultural water waste, landfill sites, and acidic leachate—has emerged as a significant problem for the global health and ecosystem. Heavy metals, such as Cd^{2+}, Hg^{2+}, Pb^{2+}, and As^{3+}, can accumulate in the body and bind with biological ligands that contain N, S, and O even at low concentrations, resulting in major negative impacts on the human health. In recent years, significant research has been conducted on developing methods for eliminating heavy-metal atoms from water. Adsorption is one of the most effective techniques for removing heavy metals from water. In the past ten years, carbon-allotrope-based nanomaterials have demonstrated significant application potential as adsorbents in various sectors.

Mashhadzadeh *et al.*[139] explained the adsorption mechanism of Gra and GDY toward heavy metals such as nickel, copper, zinc, and silver using a DFT study. To optimize the structure, nine GDY sites and three Gra sites were considered. The results indicated that Gra adsorbed nickel most strongly, with an adsorption energy of −2.791482 eV. This interaction was caused by the smaller equilibrium distance between the carbon and nickel atoms than between the other atoms. While Cu and Ag atoms were physically adsorbed to Gra, Zn was adsorbed weakly. In contrast, the nickel atom was chemically adsorbed to GDY with an adsorption energy of −3.446027 eV. Silver and copper atoms were also chemically adsorbed to GDY, but GDY showed weak physical adsorption toward zinc. Thus, GDY is a better adsorbent for heavy metals than Gra.

Liu *et al.*[140] demonstrated the complete removal of lead ions using filters composed of GDY. The Raman spectrum recorded after the lead adsorption showed a change in the peak corresponding to the acetylenic linkages in GDY, evidencing that the acetylenic linkages in GDY are responsible for metal adsorption. The Langmuir isotherm model was used to calculate the maximum adsorption capacity, which was deduced to be 470.5 mg g^{-1}. In addition, GDY fabricated on 3D copper foams could act as a filter for lead removal. In an aqueous solution containing 4.8 mg L^{-1} of lead ions, GDY exhibited an ion removal efficiency of 99.6%. Furthermore, the filter could be used for eight cycles and easily recovered *via* an acid treatment.

Currently, the detection of trace levels of heavy metals can be performed using techniques such as mass spectroscopy and atomic absorption spectroscopy. However, the use of these methods involves initial preparation and the requirement of professionals for operation. Electrochemical sensors are promising alternatives because of their simple operation, fast detection, and high sensitivity.

Li *et al.*[141] fabricated a GDY-based electrochemical sensor that could detect trace levels of Pb^{2+} and Cd^{2+} in water using techniques such as electrochemical pre-enrichment and anodic-stripping voltammetry. The detection limit for Pb^{2+} ions was 1.72 nM, whereas that for Cd^{2+} ions was 0.46 nM in the linear range of 0.01–1 μM. The GDY-modified electrode exhibited high stability, selectivity, and reproducibility. Various spectroscopic techniques have proved that the acetylenic linkages in GDY act as adsorption sites, which donate electrons for binding with heavy metal ions, thereby enhancing its electrochemical sensing capability.

Sun *et al.*[142] fabricated an ultrathin layer of GDY to increase its surface area and conductivity compared to bulk GDY. Nanostructured GDY/G was prepared and used as an electrode for electrochemical sensing. GY served as an epitaxial template for the growth of GDY with a few layers. The thin layers of GDY had a large surface area and strongly attract toxic molecules and heavy metal ions *via* π–π and d–π interactions, respectively. Hemin was further immobilized on the electrode to detect uric and ascorbic acids with high selectivity and sensitivity.

Guo *et al.*[143] used the bottom-up method to prepare *N*-substituted GDY (TGDY) as an electrode-modified material with stationary and content-controlled alkynyl bonds and pyridinic nitrogen atoms to enhance the sensing potential of GDY-based materials and better identify their detection mechanism. The addition of nitrogen in TGDY significantly improved the electrochemical performance. The signal intensity was strictly correlated with the number of detection sites in TGDY, unlike the case of *H*-substituted GDY, which is structurally similar to TGDY except for the benzene ring that was devoid of N atoms. The functionality of the TGDY-based electrochemical sensor was investigated, and the results indicated that it could detect Cd^{2+} and Pb^{2+} in water with acceptable selectivity, repeatability, stability, and application as electrochemical sensors for Cd^{2+} and Pb^{2+}. Thus, electrode materials can be synthesized and designed logically using the bottom-up approach to enhance the detection performance and investigate the detection process.

Ai *et al.*[144] used the surface of a glassy carbon electrode (GCE) to prepare a novel dendritic bismuth and GDY film. The film had a significantly large active area, high binding strength at the electrode interface, and quick electron-transfer capability. Differential pulse anodic stripping voltammetry revealed that the modified electrode served as a highly sensitive electrochemical sensor for simultaneous and individual assays of Pb(II), Cd(II), and Zn(II). Consequently, a broad linear concentration range from 10.0 nM to 100.0 M and low detection limits (0.171, 0.115, and 0.146 nM for Cd(II), Zn(II), Pb(II), respectively; S/N = 3) were achieved. The sensor had high repeatability, reproducibility, and stability and could detect real saltwater samples with a high sensitivity.

Although GDY has proved to be a promising material for metal removal, its high production cost would correspondingly elevate the price of the end product. This aspect must be researched further because at present, despite its better performance, it would be more expensive and less economical to adopt GDY as a replacement for its commercially available counterparts.

3.4. GDY for organic-pollutant removal

Organic pollutants pose a significant worldwide challenge owing to their harmful effects on plants, animals, and humans. However, researchers are using GDY-based systems composed of advanced materials to effectively remedy these pollutants from water/wastewater, on a global level. Hydrophobic interactions play a major role in the adsorptive removal of organic pollutants from aqueous water bodies, accompanied by hydrogen bonding, hydrophobic interactions, and π–π interactions.[145] Moreover, GDY can undergo strong π–π interactions with the aromatic ring-rich π-electrons of most organic pollutants, especially dyes and pesticides. This subsection presents some applications of GDY-based systems in contaminant exclusion from wastewater.

Zhu *et al.*[145] used six transition-metal salts, including Pd and Cu salts, as catalysts in a coupling reaction to produce GDY with various shapes. The procedure was direct, safe, simple, and appropriate for mass production. $CuSO_4$-catalyzed GDY had a greater yield (>90%), a lower density, and a fewer flaws. Additionally, it effectively removed organic pollutants such as tetracycline, antibiotics, dyes, and neonicotinoid pesticides from water, thereby proving the universality of the adsorption material. In particular, the adsorption effect of GDY on dye was stronger than that of traditional adsorbents such as *G* and activated carbon and comparable to that of multiwalled CNTs. This work opens up opportunities for the commercial synthesis of GDY and its promising use in eliminating organic contaminants.

Thangavel *et al.*[146] developed a novel hydrothermally synthesized GDY–ZnO nanohybrid and investigated its photocatalytic capabilities for rhodamine B and methylene blue degradation. The absorption spectra and total organic carbon studies revealed that the GDY–ZnO nanohybrids had better photocatalytic capabilities than pure ZnO nanoparticles. Additionally, in the photodegradation of both the azo dyes, the rate constant of the GDY–ZnO nanohybrids was approximately two times higher than that of the pristine ZnO nanoparticles. Owing to the possibility of generating an impurity band edge in the GDY–ZnO nanohybrid, which would allow for a more efficient movement of electrons from the valence band to the conduction band, GDY was more advantageous than Gra. Because of the conductive behavior of GDY, the photogenerated electrons were easily transferred from ZnO to GDY, reducing the recombination probability of the charged ions. The captured electrons on GDY formed superoxide radicals upon reacting with dissolved oxygen, whereas the holes generated hydroxyl radicals upon reacting with water, decomposing the azo dyes.

Thus, several catalysts can be loaded onto GDY as supports, which can aid in degrading organic pollutants. Table 4 lists various synthesis techniques for GDY-supported catalysts.

Zhang *et al.*[166] synthesized sulfur-doped GDY (SGDY) nanosheets using a simple one-pot hydrothermal method, which exhibited exceptional piezoelectric and peroxidase-like properties. Kinetic studies demonstrated that ultrasonic irradiation increased the peroxidase-like activity of SGDY; the DFT calculations explained the promotion of peroxidase activity due to the piezoelectric effect. Studies on the ability of SGDY to fight bacteria and degrade dyes and medicines concluded that it has significant potential for wastewater treatment. Additionally, a proof-of-concept system for continuous wastewater treatment was designed at a laboratory scale to demonstrate the practical applications of piezoelectric-augmented nanozymes. This work clarified the mechanism of the nanozyme/piezocatalysis coupling process, thereby providing a fresh approach to the

Table 4 Some experiments for loading catalysts onto a GDY support. Reproduced with permission from Song *et al.*,[147] Copyright 2020, Elsevier Science Ltd

Catalyst	Loading method	Reactants	Reaction conditions	Ref.
TiO_2/GDY	Hydrothermal method	GDY, TiO_2nanoparticles (NPs)	120 °C, 3 h	44
TiO_2/GDY	Hydrothermal method	GDY, TiO_2NPs	120 °C, 3 h	148
ZnO/GDY	Hydrothermal method	GDY, $Zn(OAc)_2$, NaOH	180 °C, 24 h	146
N-doped TiO_2/GDY	Hydrothermal method	GDY, N-doped TiO_2NPs	120 °C, 3 h	149
$NiCo_2S_4$ nanowires/GDY	Hydrothermal method	GDY, $Ni(NO_3)_2$, $Co(NO_3)_2$, urea Ni–Co-precursor/GDY, Na_2S	120 °C, 8 h 160 °C, 8 h	150
Ni–Fe–LDH/GDY	Hydrothermal method	GDY, $NiSO_4$, $FeSO_4$, urea, trisodium citrate	180 °C, 12 h	151
Ni–Fe–LDH/GDY	Hydrothermal method	GDY, $Ni(NO_3)_2$, $Fe(NO_3)_3$, urea, trisodium citrate	150 °C, 20 h	152
Mo^0/GDY	Hydrothermal method	GDY, Na_2MoO_4	120 °C, 12 h	153
g-C_3N_4/GDY	Solvothermal method (*N*-methyl pyrrolidone, NMP)	GDY, g-C_3N_4	50 °C, 10 h	154
CdS/GDY	Solvothermal method (dimethyl sulfoxide, DMSO)	GDY, $Cd(AcO)_2$, DMSO	180 °C, 12 h	155
WS_2/GDY	Solvothermal method (dimethyl formamide, DMF)	GDY, WCl_6, thioacetamide	120 °C, 12 h	156
CoN_x/GDY	GDY *in situ* growth	CoN_x nanosheets, HEB, pyridine	110 °C, 10 h	157
Iron carbonate hydroxide/GDY	GDY *in situ* growth	Iron carbonate hydroxide, HEB, pyridine	N_2, 60 °C, 72 h	158
MoS_2/GDY	GDY *in situ* growth	MoS_2 nanosheets, HEB, pyridine	Ar, 50 °C, 15 h, in the dark	159
Ni^0/GDY	Electrochemical deposition	GDY, $NiSO_4$	10 mA cm^{-2}, 150 s	160
Fe^0/GDY	Electrochemical deposition	GDY, $FeCl_3$	10 mA cm^{-2}, 250 s	160
Ni–Fe–LDH/GDY	Electrochemical deposition	GDY, $Ni(NO_3)_2$, $FeSO_4$	−1.0 V *versus* SCE, 90 s	161
Pd^0/GDY	Electrochemical deposition	GDY, $PdCl_2$	2 mA cm^{-2}, 10 s	162
Ag/AgBr/GO/GDY	Oil-in-water microemulsion method	GO/GDY suspension, $AgNO_3$, cetyl trimethyl ammonium bromide (CTAB) in chloroform	Room temperature, dropwise addition of oil to water within ∼5 min	163
g-C_3N_4/GDY	Calcination method	GDY, g-C_3N_4	400 °C, 2 h	164
Co NPs wrapped by N-doped carbon/GDY	Sequential annealing treatments	GDY, $Co(AcO)_2$, dicyandiamide	Ar, 500 °C, 2 h Ar, 700 °C, 2 h	165
Pt NPs/GDY	Microwave-assisted reduction	GDY, chloroplatinic acid	400 W, 160 °C, 2 min	165

rational development of highly active nanozymes for bacterial disinfection and wastewater treatment industries.

Zhu *et al.*[167] used oxygen-defective GDY under different conditions for the adsorption of pesticides from water, and it demonstrated exceptional adsorption characteristics for seven sulfonylurea herbicides (SUHs). Graphdiyne exhibited a maximum adsorption capacity of 795.51 mg g^{-1} for iodosulfuron-methyl sodium, approximately 130 times greater than previously published values for modified biochar (1.5 mg g^{-1}) and modified Gra oxide (6 mg g^{-1}). The Langmuir isotherm and pseudo-second-order kinetic models effectively fit the experimental results. The thermodynamic findings demonstrated that the adsorption process was endothermic, physical, and spontaneous. Further investigations confirmed that hydrogen bonding, hydrophobic interactions, and π–π interactions contribute significantly to the adsorption of SUH to GDY. The removal of SUHs from aqueous solutions demonstrates that oxygen-defective GDY is a highly effective, long-lasting, and interference-free adsorbent.

Shahali *et al.*[168] examined the electrical characteristics of Si-doped GDY (SiGDY) and pristine GDY nanosheets using first-principles calculations. Additionally, the adsorption energy, charge transfer, and EC were studied in relation to the adsorption of the medicine thiotepa (TPA) on the surfaces of both GDY and SiGDY sheet materials. Pristine GDY exhibited a slight adsorption capability toward TPA. In addition, after the adsorption of TPA to the GDY surface, the bandwidth energy changed by approximately 7.85%. The adsorption energy of TPA to SiGDY was approximately −18.75 kcal mol^{-1} in the gaseous phase and −49.39 kcal mol^{-1} in the aqueous phase. The solvation energy indicates the solubility of TPA in the water phase. Considerable charge transfer between SiGDY and TPA, which delivers silicon with substantial positive charges, is requirement for TPA adsorption with suitable binding energies. Furthermore, unlike pristine GDY, SiGDY could be electronically detected upon adding TPA, increasing the EC of SiGDY by approximately 20.62%.

Zhang *et al.*[169] suggested combining GDY with MIL-100(Fe) (Fe-GDY3@MIL(Fe)) to synthesize a Z-scheme photocatalyst for the degradation of dinotefuran. Owing to the confinement of GDY for Fe anchoring, a distinct C=C–Fe|O interface was formed between Fe–MOF (metal–organic framework) and Fe–GDY. The Fe–GDY3@MIL(Fe) composite with a tight C=C–Fe|O interface showed dispersed Fe sites and a highly conductive Z-scheme structure, which could effectively increase the redox ability and accelerate the cycle of converting Fe(III) to Fe(II). Thus, under the same conditions, Fe–GDY3@MIL(Fe) demonstrated 7–80 times faster mineralization kinetics and 2–5 times faster degradation kinetics than state-of-the-art catalysts. Additionally, the quick charge separation increased the stability and photocorrosion resistance of MIL-100 (Fe), thereby significantly increasing its catalytic stability and lifetime.

Chemical warfare agents (CWAs) are the deadliest and most poisonous chemicals to date. Many of these agents were dumped into the waters after World War II, posing devastative threats to marine life and other dependent species. These substances were employed in terrorist acts in the 20th century to cause a greater harm. In addition, CWAs have been widely used in various sectors: production of pesticides, dyes, and pharmaceuticals; metal cleaning; organic synthesis; and mineral refinement. Owing to their widespread use in manufacturing materials, the atmospheric concentration of CWAs has gradually increased, posing a major threat to life. Based on their target site, CWAs can be divided into four classes: blood, blistering, pulmonary, and nerve agents. Sajid *et al.*[170] tested the potential of GDY nanoflakes in electrochemical sensing of dangerous CWAs such as A-234, A-232, and A-230 and conducted theoretical investigations. The authors explained the trend of A-series CWA adsorption to GDY nanoflakes using the DFT framework. Optimized geometries, basis set superposition error-corrected energies, symmetry adapted perturbation theory (SAPT0), reduced density gradient (RDG), frontier molecular orbital, quantum theory of atoms in molecules (QTAIM), natural bond orbital (CHELPG) charge transfer, and UV-vis spectroscopy were implemented to characterize the adsorption. The computed counterpoise adsorption energies of the studied compounds ranged from 13.70–17.19 kcal mol^{-1}, demonstrating that the analytes were physically bound to GDY, which often involves noncovalent interactions. The SAPT0, RDG, and QTAIM tests further supported the noncovalent adsorption of CWAs to GDY. These characteristics also reveal the dominance of dispersion factors in complexes, including numerous noncovalent components. The sensitivity (%) and average energy gap fluctuations were evaluated from the energies of the lowest unoccupied and highest occupied molecular orbitals to estimate the sensitivity of GDY. The results of UV-vis spectroscopy, CHELPG charge transfer, and density of states (DOS) tests showed that GDY had a strong adsorption affinity for such hazardous CWAs.

The concluding remark to the previous subsection, which highlighted the cost of GFY-based materials, is valid here as well, necessitating further studies to ease the commercialization of GDY-based wastewater treatment systems.

3.5. GDY for radioactive-pollutant removal

The removal of radioactive contaminants from surface water systems and nuclear power effluents is of paramount importance. Graphdiyne-based systems are relevant because they can effectively interact with radionuclides: the sp-hybridized carbon atoms of GDYs can interact with empty metal atoms, thereby intercepting them both as desalination membranes and adsorbents.

Solar vapor generation is a promising low-energy approach to address the freshwater crisis. Pure water can be extracted from abundant seawater, wastewater, and water contaminated with heavy metal ions. Various materials and structural design

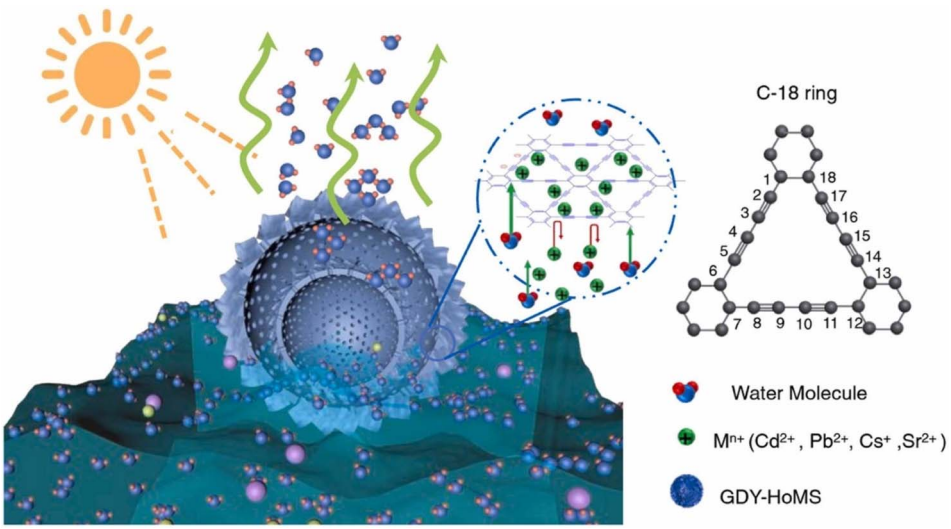

Fig. 26 Schematic of the C18 ring of GDY and the highly efficient solar vapor generation process using GDY–HoMS. The HoMS exhibits enhanced light adsorption, water transport properties, and ability to reduce the vaporization enthalpy toward achieving highly efficient photovapor generation. Moreover, the strong interaction between the metal ions and GDY contributes to the ultrahigh ion removal efficiency of the GDY–HoMS. Reproduced with permission from Zhan *et al.*[128] Copyright 2022, Elsevier Science Ltd.

stages have been proposed to achieve highly efficient steam generation, improve light absorption, optimize heat localization, and add water. In general, metal ions are significantly eliminated during evaporation, addressing another significant issue of pollutant removal from water bodies. However, a few nonvolatile metal ions may be introduced into the condensate water *via* the interactions with water molecules during evaporation. Although such conditions are considered acceptable for normal water, the water discharge requirement for radioactive water is stringent, posing further challenges to water purification. Hence, it is imperative to discover materials that can strongly interact with metal ions to reduce environmental pollution because they can bind the ions at the evaporation film and reduce the discharge quantity.

The fabrication of nanomaterials into nano-microarchitectures can aid mass transport and energy use. Typically, HoMS is crucial to each stage in the conversion of solar energy to heat: (1) light absorption, whereby light reflection and scattering are enhanced because of the large specific surface area of HoMS, which lengthens the path of light within the shell and consequently promotes the light absorption; (2) heat accumulation, by which the confined space within HoMS concentrates thermal energy to generate an outer–inner temperature gradient, which accelerates water evaporation; and (3) multiple cavities and porosity of the HoMS, which facilitate water transport (Fig. 26).[128]

The confinement effect provided by the nanopores in HoMS decreased the vaporization enthalpy by clustering water molecules during the solar vapor formation process. Meanwhile, the capillary force generated by the carefully engineered spaces between the shells facilitated water diffusion. In this regard, GDY–HoMS would be desirable for solar vapor generation owing to its high evaporation rate and good ion-removal capability. The wet-chemical bottom-up synthesis method endowed GDY with a 3D architecture, which increased the designability of the nano/microstructure. Zhan *et al.*[128] used a previously reported sequential templating approach to illustrate the sensitive design and synthesis of GDY–HoMS. The fabricated GDY–HoMS led to an increased rate of solar vapor generation with good light absorption ability, owing to the specific design.

Additionally, these ions could be confined within the C18 ring of GDY owing to their interaction with metal ions, resulting in ultrahigh ion removal efficiencies. Consequently, the evaporation rate of GDY–HoMS reached 2.7 kg m^{-2} h^{-1}. Moreover, after purification with GDY–HoMS, the amount of Cs^{+} and Sr^{2+} in the radioactive water decreased sixfold, meeting the national water discharge standard for radioactive elements; further, the amount of U(VI) in the water could meet the standard for drinking water.

In the preparation of advanced GDY-based systems for wastewater treatment toward radionuclide removal, the recyclability and reusability of the materials after each use and nonreactivity with the radionuclides after their usage must be considered.

3.6. GDY for nitrate removal

Industrial practices, such as the overuse of nitrate as a fertilizer, lead to surface and groundwater nitrate contamination. Owing to the potential health hazards due to nitrate ions, their removal from water is crucial when their concentration exceeds the permissible threshold. Current remediation techniques, such as ion exchange, adsorption, electrodialysis, and biological denitrification, separate nitrate ions from water as a soluble and stable constituent. The use of nanostructured membranes for ion removal from aqueous solutions has recently received considerable attention and has been widely studied.

Majidi *et al.*[171] conducted MD simulations and investigated the effectiveness of a pure nanoporous GDY sheet in removing nitrate ions from water. They demonstrated that water could

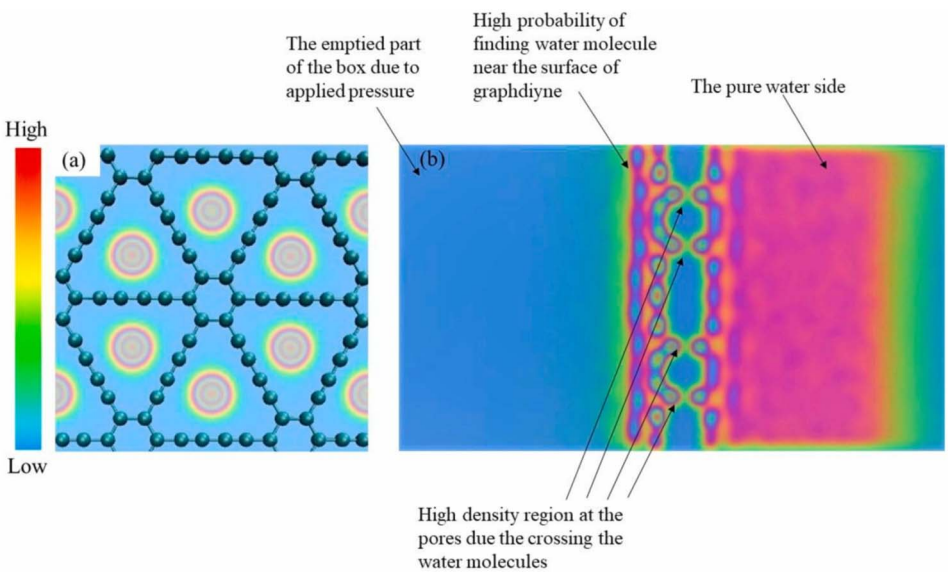

Fig. 27 (a) Water density maps inside the pores of GDY during the separation process. (b) System-wide water density map at 400 MPa. Reproduced with permission from Majidi *et al.*,[171] Copyright 2023, Elsevier Science Ltd.

cross a GDY sheet under an activated condition that could be precisely controlled by adjusting the hydrostatic pressure and external temperature. External pressure was used to obtain a nonlinear relationship for water flow rate: a high pressure of 500 MPa led to a water permeability of 6.19 L d^{-1} cm^{-2} MPa^{-1} with 100% nitrate ion rejection. The results of the PMF study supported those of the water and ion density profiles, indicating that the large free-energy barrier for the nitrate ions in the pores was sufficient to prevent them from penetrating the membrane. In contrast, the water molecules encountered a lower energy barrier in the core of the pores, allowing them to penetrate.

However, an increase in the temperature decreased the activation energy of the water molecules, which increased the water flux. The local structure of the water in the system was characterized using water density analysis, and the influence of the membrane on the structure and dynamics of the water, in the presence of the GDY membrane, was further investigated using hydrogen-bonding analysis. The two-hydrogen-bond transient structure, which promoted the transport of water molecules across the pores and served as the transition state in nature, enabled water to travel across the nanopores of GDY. The hydrophobic nature of the membrane increased the water flow because there was no attraction between the membrane and water after it penetrated the pores. This led to a high water flux, according to the water density map (Fig. 27) and the lifetime of the hydrogen bonds. However, the water molecules and the membrane did not strongly repel each other. The novel insights from this study have profound implications in controlling cellular water transport and studying water permeation in minerals with nanoscale channels.

The application of electrochemical technologies to break down nitrogen-containing contaminants from industrial wastewater to produce N_2 gas instead of NH_3 gas is an important research area in environmental protection.

Ai and Wang[172] performed DFT calculations to thoroughly examine the electrochemical nitrate reduction reaction (NO_3RR) on transition-metal single-atom-supported GDY catalysts (TM@GDY SACs). Among the studied systems, vanadium-anchored GDY (V@GDY) exhibited the lowest limiting potential of −0.63 V *versus* reversible hydrogen electrode. Owing to the relatively weak adsorption of H protons to the TM@GDY SACs, the competing hydrogen evolution reaction was suppressed substantially. In addition, considerable energy was consumed to break through the energy barrier when by-products (NO, NO_2, N_2O, and N_2) were formed on V@GDY without an additional electrode potential, demonstrating the selectivity of NH_3 in the NO_3RR process. *Ab initio* MD simulations revelated that the V@GDY catalyst exhibited exceptional structural stability at 600 K without considerable deformation, demonstrating its potential for synthesis. This study paves the way for the advancement of the NO_3RR process, in addition to providing a feasible NO_3RR electrocatalyst.

Yang *et al.*[173] conducted DFT computations and investigated the ability of GDY anchored with a sequence of single transition-metal atoms (TM/GDY) for electrocatalysis of the NO_3RR process to NH_3. Through a methodical analysis of the activity and selectivity of numerous TM/GDY candidates, Os/GDY was determined to be an appropriate catalyst for NO_3RR with a low limiting potential (0.37 V) and a strong suppressing impact on the competing reactions. The origin of the catalytic activity of NO_3RR was explained with respect to the adsorption strength and polarized charge on the adsorbed NO_3* species, and a volcano plot was obtained for the scaling relation of free adsorption energies of variable intermediates. These findings suggest a suitable electrocatalyst to increase the NO_3RR for ammonia synthesis and provide a thorough understanding of the NO_3RR process.

4. A brief comparison of water desalination efficiencies of GY/GDY materials and other materials

In addition to the aforementioned advantages, GY and GDY are excellent separation materials for desalination and water purification. They hold great promise for desalination and filtration of water because they can modify their pore architectures to facilitate the simple passage of water molecules. Moreover, their surface energy is highly tunable, and they are superhydrophobic. In contrast to GYs, GDYs are semipermeable with several continuous channels that can permit the entry of fair amount of water while efficiently rejecting ions, at certain applied pressures.[23] To increase their water permeability and salt rejection, these nanopore channels must be functionalized or negatively charged.[174] The special carbon–carbon triple bond in GY/GDY affords several important properties, including the momentum shift of their Dirac cones, leading to tunable energy gap, which favors electron mobility and consequently, surface functionalization, as stated previously (Section(s) 2.1 and 2.2).

Mass flow across neutral pores in GY is governed by the molecular sieving mechanism, which can be used to construct membranes for water pretreatment and to form ultrapure nitrogen or oxygen. Multilayer membranes can enhance GYs by adjusting the transverse distance between pores and the pore offset for use in practical applications such as desalination.[175] Although an increase in the pore offset of multilayer porous Gra boosts salt rejection, certain related technical challenges must be solved. Pore fabrication is not necessary to control the offset in multilayer structures, considering different interlayer stacking patterns, because GY has intrinsic nanopores.[175]

It would be prudent to compare the water desalination efficiency of GY/GDY with that of other materials, given that GDY exhibits a higher desalination efficiency than its source material GY[175] because of dissimilar atomic nanopores. For instance, a bilayered nanoporous Gra (NPG) desalination membrane with a nanopore size (for its upstream layer) of 3.0 Å demonstrated 100% salt rejection at various applied pressures up to ~200 MPa, whereas its downstream layer with a nanopore size of 4.5 Å exhibited 85–100% salt rejection.[175] Thus, the salt rejection of desalination membranes declines with a better pore alignment, a larger interlayer distance, and an increasing number of layers, which has a direct relationship with the salt rejection up to the threshold.

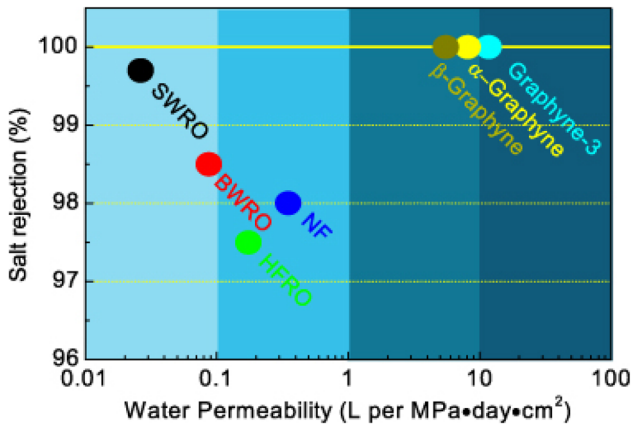

Fig. 28 Performance comparison between α-GY, β-GY, GY-3, and conventional RO desalination membranes. The three GY monolayers can desalt water at 100% ion rejection with a throughput significantly faster than commercial RO membranes such as polymeric seawater RO (SWRO), brackish water RO (BWRO), high-flux RO (HFRO), and NF.[24] Reproduced with permission from Xue *et al.*[24] Copyright 2013, IOP Science.

Cohen-Tanugi and colleagues,[175] compared the desalination (salt rejection) abilities of NPG (~200 nm thick), whose performance is close to that of GY/GDY, and commercially available polyamide films. The permeability of the NPG membrane was 2 L m^{-2} h^{-1} bar^{-1}, which is within a similar order of magnitude as that of a conventional polyamide membrane.[175] The salt rejection ability within one or a few layers and the capability of preparing ultrathin NPG sheets are suggested to be the key advantages of NPG over polyamide. In contrast, it is challenging to synthesize polyamide films with a thickness less than 100–200 nm because the film thickness is determined by the mass transfer of the diamine to the organic phase during interfacial polymerization;[176] moreover, a significantly thinner polyamide film may not exhibit sufficiently high salt rejection. Multilayer Gra will be a viable material for water desalination because it renders the NPG membranes more commercially feasible at a thickness smaller by orders of magnitude (relative to polyamide membranes), strongly suggesting that GY/GDY-based membranes would perform better.

Xue *et al.*[24] prepared and investigated five categories of graphynes; the permeability of the systems toward Cl^- and Na^+ ion (with a concentration of 1.2 M) and rejection from water were evaluated at 0–250 MPa through MD simulations. The H_2O transport in β-GY was 31% faster than in α-GY owning to its larger nanopore area, which was determined by considering the van der Waals radius of the carbon atom as 1.7 Å.[177]

Although GDY was impermeable to water or ions at a pressure of 250 MPa, GY-3 and GY-4 demonstrated higher water permeabilities than α-GY and β-GY. Moreover, α-GY, β-GY, and GY-3 completely rejected Na^+ and Cl^- salt ions. Additionally, their ion rejection ability was prevalent at high working pressures up to 250 MPa over a salt concentration range of 1.2–3.6 M, proving their independence from these factors.[177] Further, they rejected all other salt ions present in seawater, which was an anomaly because none of the ions could penetrate them. In addition, GY-4 exhibited a weaker salt rejection ability and permeated water more quickly than other GY species. The permeability of these GYs at 100% salt rejection could be two orders of magnitude higher than that of commercial RO membranes, as shown in Fig. 28, according to a performance comparison between α-GY, β-GY, GY-3, and traditional RO membranes (*i.e.*, seawater RO, brackish water RO, high-flux RO, and NF).

Functionalization is another important aspect of GY-based materials aimed at desalination applications: it facilitates out-of-plane bending of the functionalized groups.[178] The addition of hydroxyl functionalities to the GY architecture could enhance the permeation of water molecules through monolayer Gra. This alignment with water flow increased the effective pore width. Raju *et al.*[178] modified α-GY and γ(2,3,4)-GY membranes and evaluated them with respect to their pore geometry, chemical functionalization pore size, and applied pressure. The water flux results proved that the functionalized GYs outperformed their pristine forms when used as desalination membranes. They rejected more than 90% of the salts at 1 GPa.[178] Furthermore, at pressures up to 1 GPa, pores with an

Table 5 Performance comparison of various desalination membranes as per the literature

Desalination membrane	Rejected ion(s)	Ion rejection (%)	Water permeability (L cm^{-2} d^{-1} MPa^{-1})	Operating pressure (MPa)	Ref.
α-GY	Na^+, Cl^-, Mg^{2+}, K^+, and Ca^{2+}	100	8.1	0–250	24
β-GY	Na^+, Cl^-, Mg^{2+}, K^+, and Ca^{2+}	100	5.5	0–250	24
γ-GY	Na^+ and Cl^-	100	8953 L m^{-2} h^{-1} bar^{-1}	50	174
GDY	Na^+	100	—	10–30	136
GDY	Hg^{2+} and Cu^{2+}	100	6.19	5–500	171
GDY	NO_3^-	100	6.19	—	2
GY-3	Na^+, Cl^-, Mg^{2+}, K^+, and Ca^{2+}	100	11.7	0–250	24
GY-4	Na^+, Cl^-, Mg^{2+}, K^+, and Ca^{2+}	100	13–14.3	0–250	24,179
RO membrane	Na^+, Cl^-, Mg^{2+}, K^+, and Ca^{2+}	99	~0.05	0–250	24
GY-4	Na^+ and Cl^-	100	13	100	180
Gra	Na^+ and Cl^-	33–100	6	100	180
H–SiCNS	NO_3^-	84	472.6 mm ns^{-1}	50	181
F–SiCNS	NO_3^-	90	332.5 mm ns^{-1}	50	181
Polyacrylonitrile (PAN)	NO_3^-	88	27.0 L m^{-2} h^{-1}	0.4	182
Polyamide (NF270)	NO_3^- and Cl^-	60	1.5 and 4.5 L m^{-2} h^{-1} bar^{-1}	50	183

area of 20–50 Å^2 rejected more than 90% of the ions. The water permeability reached ~85 L cm^{-2} d^{-1} MPa^{-1}, up to three orders of magnitude greater than that of SWRO membranes and tenfold that of NPG membranes. Pore chemistry, functionalization, and geometry were crucial to the modulation of water flow, as inferred by the water velocity, density, and energy barriers in the pores.[178] It is worth noting that the carbon atom is not stationary in a real desalination system. However, most MD simulations of GY membrane desalination consider fixed carbon atoms in the membrane to prevent out-of-plane displacement.[177]

In another study, GY-3 exhibited a higher water flux than CNTs.[1] When $n \geq 3$, the water molecules could cross the GY-n membranes; when $n \leq 6$, ion rejection occurred. The water permeability of the GY-3 membrane was up to three orders of magnitude greater than that of conventional RO membranes and up to ten times that of NPG membranes.[23]

The applications of GY-based materials in desalination and water purification are being widely investigated; these materials offer scope in other niches as well. Desalination based on commercial RO presents a high energy demand, with the specific energy requirement being 3.6–5.7 kW h m^{-3}. In contrast, a GY-based membrane such as GY-4 required a specific energy of 3.6×10^{-3} kW h m^{-3} to produce 1 m^3 of fresh water, three orders of magnitude less than the current commercial RO membranes,[179] despite the lower water permeability compared to GY-based systems (Table 5).

5. Challenges, conclusion, and future outlook

5.1. Challenges

Despite GYs being a viable alternative to most existing advanced separation membranes and adsorbents, GDY-based adsorbents and membranes operating *via* separation mechanisms have not been experimented, especially on a commercial scale. The first step in extending the characterization of these membranes beyond theoretical predictions and experimental validations would be to realize that GY membranes are in the early developmental stage. Experimental proof-of-concept devices, lab-scale adsorbents/membranes, and industrial-scale adsorbents/membranes with sufficient stability and cost-effectiveness could be developed as a part of the GY-based membrane technology. The key difficulties include accurate computational characterization of GY separation performance and high-quality production and maintenance of the structural robustness of GYs.

Fabricating high-quality, large-area GY materials is the first step in developing GY-based systems for wastewater treatment, followed by proof-of-concept tests in the lab and then by a scale-up and feasibility for the industry. The quality of GY is the most crucial parameter of GY-based systems, especially in membrane applications, because flaws such as vacancies, rips, and wrinkles can reduce the separation efficiency. The mechanical strength of newly constructed GYs should be transferred to the supporting porous substrates such that they can endure loading pressures. In the manufacturing of Gra, chemical or mechanical exfoliation, a commonly implemented top-down technique, can produce a sheet consisting of one or a few layers directly from raw graphite. However, GYs cannot be synthesized using this top-down method because no bulk phase is available as per the experiments. Alternatively, a molecular level bottom-up approach of starting from precursor molecules containing acetylenic linkages can be implemented. If we had an enough precursor, we could construct a 2D extended structure by carefully controlling the chemical processes among the precursor molecules. Graphdiyne substructures or subunits with more than four structural units can be produced only *via* conventional organic synthesis because of the laborious synthesis procedures (such as metal-catalyzed cross-coupling processes, alkyne metathesis, and templated synthesis), limited production rates, and poor solubilities.[11] The effective fabrication of 2D Gra sheets with a thickness of 1 μm *via* the cross-coupling reaction on Cu foil surfaces with HEB as a precursor was a breakthrough in Gra synthesis by Li *et al.* in 2010.[41] The Cu foil provided both the reaction substrate and Cu^{2+} ions necessary to catalyze the cross-coupling process. The as-prepared uniform GDY films were composed of GDY multilayers. A linked monolayer carbon network could be constructed using acetylenic scaffoldings, analogs of Gra, by chemical vapor deposition (CVD) using HEB as the precursor.[184] However, a TEM scan of the resultant film revealed little to no in-plane order in the structure over the examined region. Through the CVD approach, a logical design of the catalytic environment, including the temperature and substrate preprocessing, is required to fabricate well-ordered molecular structures over broad areas, such as GDY. Liu and Zhang *et al.* used Gra as a surface template to prepare a continuous flat ultrathin GDY film with a thickness of less than 3 nm (6–10 layers).[185] They also developed GDY-based field-effect transistor (FET) devices from hexagonal boron nitride using this templating approach. However, the carrier mobility (under specific electric fields, carrier mobility is a measure of the speed of electrons or holes) of the FET was lower than that anticipated theoretically. This finding emphasizes the necessity of refining the templating process to increase domains and decrease flaws for enhancing the quality of GDY. Matsuoka *et al.* reported a bottom-up synthesis of crystalline GDY nanosheets *via* a liquid–liquid or gas–liquid interfacial technique using HEB as the precursor.[186] The resulting single-crystal Gra nanosheets had regular hexagonal domains with a uniform thickness of 3.0 nm and lateral dimensions of 1.5 μm. Numerous papers have reviewed the experiments on the manufacturing of GDY, including those detailed herein.[187] Despite the significant advancements, the fabrication of monolayer Gra remains difficult. Moreover, the preparation of other members of the GY family, especially those useful for desalination (such as GY, GDY, and GY-3), present difficulties. The challenging synthesis of appropriate precursors is one contributing factor. Recently, Li *et al.* prepared a thin film containing-GY with a thickness of approximately 25 nm on a copper foil using a modified Glaser–Hay coupling procedure, after synthesizing the precursor molecule tetraethynylethene.[188] It is reasonable to predict that

advancements in GY material preparation will result from surface engineering of substrates, careful design and synthesis of new precursors used in cross-coupling reactions, and innovations in preparation procedures. A thorough microscopic understanding of the reaction process and the mechanism involved in the formation of such 2D materials should be able to assist in experimental efforts, especially from a theoretical standpoint.

Maintaining sufficient mechanical strength in GYs to prevent mechanical failures during the clamping process in the manufacturing of membrane modules and to sustain high operating pressures during the separation processes is another challenge. Additionally, the stiffness of GY is crucial because excess tensile deformation may result in considerable pore expansion in GYs, impacting the separation performance. Graphyne structures typically have a high stiffness and mechanical strength.[110] With an increase in the number of acetylenic groups, the fracture strain remains constant but the Young's modulus decreases.[110] Zhao *et al.* compared the mechanical characteristics of GDY and a few carbon allotropes. They emphasized the dominance of area density (*i.e.*, the quantity of carbon atoms per unit area) in influencing the mechanical characteristics.[189] Lin and Buehler reported MD-based biaxial mechanical tensile tests on a series of GY-*n* (n = 3–6) membranes; the ultimate stress and strain ranged 16.7–32.3 GPa and 1.2–2.7%, respectively. These values are significantly higher than those of conventional polymer-based membranes and are comparable to those of carbon nanotubes, which have an ultimate stress of 11–63 GPa.[190] In particular, among the GYs under consideration, GY-3 has the best mechanical properties, deeming it an excellent choice for desalination membranes. While assessing the effect of mechanical deformation on the desalination performance of GY-3, the water permeance of the membrane increased slightly; however, the rate of salt rejection remained unaffected.[190] Structural stability in both air and water is essential for using GYs in membrane applications. In theory, acetylenic linkages in GY would make it less stable than other allotropes that resemble sp^2 Gra. Additional research is required on this topic, particularly in relation to the membrane separation processes. Although the aforementioned research suggests that pristine Gra is a promising candidate for mechanically robust membrane materials, its mechanical properties may significantly deteriorate in practical applications because the synthesized Gra typically contains flaws and adsorbed impurities introduced during the fabrication, transfer, and integration processes. In addition, introducing functionalization to control its separation performance would affect its mechanical properties. In this regard, additional theoretical and practical work are necessary for resolving these problems and consequently, direct the development of GY-based membranes. However, when GY is appropriately supported by a porous substrate, which is typical of existing commercial membrane modules, it may sustain high loading pressures. Cohen-Tanugi and Grossman anticipated that in the case of Gra, a porous membrane atop a porous substrate with pores smaller than 1 μm could tolerate a loading pressure of 57 MPa, which is roughly tenfold higher than that used in commercial RO desalination.[191] However, the supported Gra has different chemical bonds, which may result in discrepancies in the strength data. Because a monolayer Gra with a large surface area and high quality has not been experimentally demonstrated yet, its true mechanical strength is yet to be determined. Nevertheless, the GY membranes may require strengthening. Further research is required for optimizing the structural layout of the porous substrate layer and improving its adhesion to GYs to fabricate mechanically robust membrane modules, highlighting the necessity for additional thorough theoretical studies. For example, an MD study revealed that GY-4 could achieve complete salt rejection while exhibiting a higher water permeance than GY-3;[23] however, another study demonstrated that GY-4 achieves only partial salt rejection, especially when subjected to high pressures.[25] Therefore, systematic theoretical investigations are required to determine the dependence of the expected performance on these characteristics. Differences in the choice of the water model and strategies for pressure loading may account for this inconsistency. Accurate determination of permeance and selectivity is another issue with computational methods. On the one hand, MD simulations could predict permeance with a high accuracy if numerous permeation events of the desired species are provided; however, they could not predict the high selectivity with ease because there were not many permeation events of the undesirable species. On the other hand, DFT calculations could forecast an exceptionally high selectivity based on the energy landscape;[8] however, they neglected the impact of molecular population and variations in temperature and pressure, which are relevant to real-world systems. These challenges may be overcome by integrating the existing methods (*e.g.*, QM/MD) or implementing new computational methods.

5.2. Conclusion and future outlook

5.2.1. Conclusions. To this end, we have presented herein an extensive overview of the synthesis of GY and GDY, the history of GDY, its properties, and its applications in wastewater/water remediation through adsorption and desalination. This review would benefit researchers working on GDYs and its wastewater remediation applications. The synthesis and application of GYs and GDYs in water/wastewater remediation have been reported in recent decades, including the challenges in the field. A significant challenge faced by researchers/industrialists is the difficulty in the bulk synthesis of GY and GDY; intensive research is being conducted in this respect to find a solution. Other concerns include the complexity of controlling the synthesis process parameters, production cost, and environmental friendliness of the synthesis processes.

The limited application or use of GDY in excluding radioactive contaminants from water/wastewater is yet another concern. An effective design/fabrication, followed by the application of GDYs rich in diverse surface functionalities and comprising a π-electron-rich surface to water purification could significantly address the pressing issue of vast load of wastewater contaminants, especially radionuclides, heavy metals, pesticides, and toxic dyes.

5.2.2. Future outlook. Devising inexpensive, simple, and practical methods for synthesizing eco-friendly GYs and GDYs would pave the way for commercial manufacturing GY and GDY. Synthesis of highly effective, recyclable, self-cleaning (readily releasing the adsorbed or retained contaminants), biodegradable adsorbents and desalination membranes/systems deserves a special focus.

The molecular sieving mechanism governs the mass transport through neutral GY pores, which can be used to design membranes for water pretreatment and ultrapure nitrogen or oxygen production.

The modification of the transverse distance between the pores and the pore offset in multilayer membranes can enhance the suitability of GYs for practical applications such as desalination.[175] The salt rejection of multilayer porous Gra can be improved by increasing the pore offset; however, certain technical obstacles must be overcome. Because GY already contains intrinsic nanopores, no additional pore manufacturing is required to control the offset in multilayer structures, considering the varied interlayer stacking arrangements. A multilayer sheet of graphtriyne (GY-3) can be successfully constructed, as shown by DFT simulations, and the best structures reported thus far possessed ABA-stacked patterns with an average interlayer spacing of ~3.45 Å.[192] The lateral pore offset or the displacement of a layer from its neighboring layers was ~1.6 Å. Light gas species such as CO_2, N_2, H_2O, and H_2 were permeable through the nanochannels formed by the spatial link between pores on various sheets.[192] The desalination performances of GY-3 and GY-4 in a bilayered configurations (AA- and AB-stacking) were analyzed by Akhavan *et al.*[193] They discovered that bilayered GY-4 exhibited a higher salt rejection than monolayered GY-4 .[193] The highest water permeability corresponded to a spacing of ~3.5 Å, and the difference in the water permeability between AA- and AB-stacked GY-3 was small for less spacing but large for greater spacing. Further research is warranted for the optimization of the separation performance.

The tunability of molecular properties and number of layers in synthesized GDY-based systems intended for water remediation through desalination/filtration or adsorption will significantly influence the overall performance of the GDY-based systems.

Conflicts of interest

The authors declare no conflicts of interest.

Acknowledgements

The authors would like to acknowledge the financial support from the Department of Science and Innovation (C6ACH77), Council for Scientific and Industrial Research, Pretoria (086ADMIN), and University of Johannesburg (086310), South Africa.

References

1 J. Kou, X. Zhou, Y. Chen, H. Lu, F. Wu and J. Fan, *J. Chem. Phys.*, 2013, **139**, 064705.
2 S. Majidi, H. Erfan-Niya, J. Azamat, E. R. Cruz-Chú and J. H. Walther, *J. Phys. Chem. B*, 2021, **125**, 12254–12263.
3 A. Zaman, J. Chakraborty, S. Santra, B. Gabi, J. T. Orasugh, P. Banerjee and D. Chattopadhyay, in *Membranes for Water Treatment and Remediation*, ed. A. K. Nadda, P. Banerjee, S. Sharma and P. Nguyen-Tri, Springer Nature Singapore, Singapore, 2023, pp. 157–208, DOI: **10.1007/978-981-19-9176-9_7**.
4 (*a*) H. Mittal, S. M. Alhassan and S. S. Ray, *J. Environ. Chem. Eng.*, 2018, **6**, 7119–7131; (*b*) M. S. Ali, J. T. Orasugh, S. S. Ray and D. Chattopadhyay, in *Development in Wastewater Treatment Research and Processes*, ed. M. P. Shah, S. Rodriguez-Couto, A. Kumar Nadda and A. Daverey, Elsevier, 2023, pp. 61–77, DOI: **10.1016/B978-0-323-88505-8.00011-5**.
5 H. Kroto, *Astrophys. J.*, 1987, **314**, 352.
6 S. Iijima and T. Ichihashi, *Nature*, 1993, **363**, 603–605.
7 J. T. Orasugh and S. S. Ray, *ACS Omega*, 2022, **7**, 33699–33718.
8 J. T. Orasugh and S. S. Ray, *Polymers*, 2022, **14**, 704.
9 L. Shi, P. Rohringer, K. Suenaga, Y. Niimi, J. Kotakoski, J. C. Meyer, H. Peterlik, M. Wanko, S. Cahangirov and A. Rubio, *Nat. Mater.*, 2016, **15**, 634–639.
10 R. Baughman, H. Eckhardt and M. Kertesz, *J. Chem. Phys.*, 1987, **87**, 6687–6699.
11 M. M. Haley, S. C. Brand and J. J. Pak, *Angew. Chem., Int. Ed. Engl.*, 1997, **36**, 836–838.
12 Y. Li, L. Xu, H. Liu and Y. Li, *Chem. Soc. Rev.*, 2014, **43**, 2572–2586.
13 Z. Chen, C. Molina-Jirón, S. Klyatskaya, F. Klappenberger and M. Ruben, *Ann. Phys.*, 2017, **529**, 1700056.
14 A. Hirsch, *Nat. Mater.*, 2010, **9**, 868–871.
15 M. M. Haley, *Pure Appl. Chem.*, 2008, **80**, 519–532.
16 H. Zhan, Y. Zhang, J. M. Bell, Y.-W. Mai and Y. Gu, *Carbon*, 2014, **77**, 416–423.
17 A. L. Ivanovskii, *Prog. Solid State Chem.*, 2013, **41**, 1–19.
18 J. Kang, J. Li, F. Wu, S.-S. Li and J.-B. Xia, *J. Phys. Chem. C*, 2011, **115**, 20466–20470.
19 M. Long, L. Tang, D. Wang, Y. Li and Z. Shuai, *ACS Nano*, 2011, **5**, 2593–2600.
20 J. Wang, S. Zhang, J. Zhou, R. Liu, R. Du, H. Xu, Z. Liu, J. Zhang and Z. Liu, *Phys. Chem. Chem. Phys.*, 2014, **16**, 11303–11309.
21 Y. Pei, *Phys. B Condens. Matter*, 2012, **407**, 4436–4439.
22 M. Becton, L. Zhang and X. Wang, *Phys. B Condens. Matter*, 2014, **16**, 18233–18240.
23 C. Zhu, H. Li, X. C. Zeng, E. Wang and S. Meng, *Sci. Rep.*, 2013, **3**, 3163.
24 M. Xue, H. Qiu and W. Guo, *Nanotechnology*, 2013, **24**, 505720.
25 J. Kou, X. Zhou, H. Lu, F. Wu and J. Fan, *Nanoscale*, 2014, **6**, 1865–1870.
26 X. Tan, L. Kou, H. A. Tahini and S. C. Smith, *Mol. Simulat.*, 2016, **42**, 573–579.
27 M. Bartolomei, E. Carmona-Novillo, M. I. Hernández, J. Campos-Martínez, F. Pirani, G. Giorgi and K. Yamashita, *J. Phys. Chem. Lett.*, 2014, **5**, 751–755.

28 Y. Liu, *Acta Chim. Sin.*, 2013, **71**, 260.
29 Z. Lu, S. Li, P. Lv, C. He, D. Ma and Z. Yang, *Appl. Surf. Sci.*, 2016, **360**, 1–7.
30 X. Chen, P. Gao, L. Guo and S. Zhang, *Sci. Rep.*, 2015, **5**, 1–9.
31 (*a*) G. H. Mhlongo, D. E. motaung, F. R. Cummings, H. C. Swart and S. S. Ray, *Sci. Rep.*, 2019, **9**, 9881; (*b*) J. Li, C. Wan, C. Wang, H. Zhang and X. Chen, *Chem. Res. Chin. Univ.*, 2020, **36**, 622–630; (*c*) M. Biswas and S. S. Ray, *J. Appl. Polym. Sci.*, 2000, **77**, 2948–2956.
32 R. H. Baughman, H. Eckhardt and M. Kertesz, *J. Chem. Phys.*, 1987, **87**, 6687–6699.
33 M. M. Haley, S. C. Brand and J. J. Pak, *Angew. Chem., Int. Ed. Engl.*, 1997, **36**, 835–838.
34 R. H. Baughman, D. S. Galvão, C. Cui, Y. Wang and D. Tománek, *Chem. Phys. Lett.*, 1993, **204**, 8–14.
35 V. R. Coluci, S. F. Braga, S. B. Legoas, D. S. Galvão and R. H. Baughman, *Nanotechnology*, 2004, **15**, S142.
36 N. Narita, S. Nagai, S. Suzuki and K. Nakao, *Phys. Rev. B: Condens. Matter Mater. Phys.*, 2000, **62**, 11146–11151.
37 A. N. Enyashin, Y. N. Makurin and A. L. Ivanovskii, *Carbon*, 2004, **42**, 2081–2089.
38 A. N. Enyashin, V. V. Ivanovskaya, Y. N. Makurin and A. L. Ivanovskii, *Dokl. Phys. Chem.*, 2004, **395**, 62–66.
39 V. V. Ivanovskaya, A. N. Enyashin and A. L. Ivanovskii, *Russ. J. Phys. Chem. A*, 2006, **80**, 372–379.
40 R. D. Kennedy, D. Lloyd and H. McNab, *J. Chem. Soc., Perkin Trans. 1*, 2002, **2**, 1601–1621.
41 G. Li, Y. Li, H. Liu, Y. Guo, Y. Li and D. Zhu, *Chem. Commun.*, 2010, **46**, 3256–3258.
42 X. Qian, Z. Ning, Y. Li, H. Liu, C. Ouyang, Q. Chen and Y. Li, *Dalton Trans.*, 2012, **41**, 730–733.
43 H. Du, Z. Deng, Z. Lü, Y. Yin, L. Yu, H. Wu, Z. Chen, Y. Zou, Y. Wang, H. Liu and Y. Li, *Synth. Met.*, 2011, **161**, 2055–2057.
44 S. Wang, L. Yi, J. E. Halpert, X. Lai, Y. Liu, H. Cao, R. Yu, D. Wang and Y. Li, *Small*, 2012, **8**, 265–271.
45 G. Li, Y. Li, X. Qian, H. Liu, H. Lin, N. Chen and Y. Li, *J. Phys. Chem. C*, 2011, **115**, 2611–2615.
46 Y. Li, L.-Q. Song, M. Q. Chen, Y.-M. Zhang, J. Li, X.-Y. Feng, W. Li, W. Guo, G. Jia, H. Wang and J. Yu, *Ann. Biomed. Eng.*, 2012, **40**, 2611–2618.
47 D. Malko, C. Neiss, F. Viñes and A. Görling, *Phys. Rev. Lett.*, 2012, **108**, 086804.
48 H.-J. Cui, X.-L. Sheng, Q.-B. Yan, Q.-R. Zheng and G. Su, *Phys. Chem. Chem. Phys.*, 2013, **15**, 8179–8185.
49 S. W. Cranford and M. J. Buehler, *Carbon*, 2011, **49**, 4111–4121.
50 R. C. Andrew, R. E. Mapasha, A. M. Ukpong and N. Chetty, *Phys. Rev. B: Condens. Matter Mater. Phys.*, 2012, **85**, 125428.
51 H. Zhang, M. Zhao, X. He, Z. Wang, X. Zhang and X. Liu, *J. Phys. Chem. C*, 2011, **115**, 8845–8850.
52 L. D. Pan, L. Z. Zhang, B. Q. Song, S. X. Du and H. J. Gao, *Appl. Phys. Lett.*, 2011, **98**, 173102.
53 H. J. Hwang, Y. Kwon and H. Lee, *J. Phys. Chem. C*, 2012, **116**, 20220–20224.
54 W.-h. Zhao, L.-f. Yuan and J.-l. Yang, *Chin. J. Chem. Phys.*, 2012, **25**, 434–440.
55 J. J. He, S. Y. Ma, P. Zhou, C. X. Zhang, C. Y. He and L. Z. Sun, Magnetic Properties of Single Transition-Metal Atom Absorbed Graphdiyne and Graphyne Sheet from DFT plus U Calculations, *J. Phys. Chem. C*, 2012, **116**, 26313–26321.
56 A. N. Enyashin and A. L. Ivanovskii, *Superlattices Microstruct.*, 2013, **55**, 75–82.
57 A. T. Balaban, C. C. Rentia and E. Ciupitu, *Rev. Roum. Chim.*, 1968, **13**, 231–247.
58 L. P. Biró, G. I. Márk, Z. E. Horváth, K. Kertész, J. Gyulai, J. B. Nagy and P. Lambin, *Carbon*, 2004, **42**, 2561–2566.
59 A. A. Karenin, *J. Phys. Conf. Ser.*, 2012, **345**, 012025.
60 V. H. Crespi, L. X. Benedict, M. L. Cohen and S. G. Louie, *Phys. Rev. B: Condens. Matter Mater. Phys.*, 1996, **53**, R13303–R13305.
61 H. Terrones, M. Terrones, E. Hernández, N. Grobert, J. C. Charlier and P. M. Ajayan, *Phys. Rev. Lett.*, 2000, **84**, 1716–1719.
62 B. S. Pujari, A. Tokarev and D. A. Saraf, *J. Condens. Matter Phys.*, 2012, **24**, 175501.
63 D. Malko, C. Neiss, F. Viñes and A. Görling, *Phys. Rev. Lett.*, 2012, **108**, 086804.
64 V. Coluci, S. Braga, S. Legoas, D. Galvao and R. Baughman, *Phys. Rev. B: Condens. Matter Mater. Phys.*, 2003, **68**, 035430.
65 P. Serafini, A. Milani, D. M. Proserpio and C. S. Casari, *J. Phys. Chem. C*, 2021, **125**, 18456–18466.
66 M. Kondo, D. Nozaki, M. Tachibana, T. Yumura and K. Yoshizawa, *Chem. Phys.*, 2005, **312**, 289–297.
67 M. Iyoda, J. Yamakawa and M. J. Rahman, *Angew. Chem., Int. Ed.*, 2011, **50**, 10522–10553.
68 F. Diederich and M. Kivala, *Adv. Mater.*, 2010, **22**, 803–812.
69 T. Lin and J. Wang, *ACS Appl. Mater. Interfaces*, 2019, **11**, 2638–2646.
70 L. Sun, P. H. Jiang, H. J. Liu, D. D. Fan, J. H. Liang, J. Wei, L. Cheng, J. Zhang and J. Shi, *Carbon*, 2015, **90**, 255–259.
71 A. Rajabpour, S. Vaez and M. Jalalvand, *Proceedings of the 5th International Conference on Nanostructures (ICNS5) 6-9 March 2014*, Kish Island, Iran.
72 Y. Wan, S. Xiong, B. Ouyang, Z. Niu, Y. Ni, Y. Zhao and X. Zhang, *ACS Omega*, 2019, **4**, 4147–4152.
73 A. R. Puigdollers, G. Alonso and P. Gamallo, *Carbon*, 2016, **96**, 879–887.
74 S. Wang, Y. Si, J. Yuan, B. Yang and H. Chen, *Phys. Chem. Chem. Phys.*, 2016, **18**, 24210–24218.
75 Y. Zhang, Q. Pei and C. Wang, *Appl. Phys. Lett.*, 2012, **101**, 081909.
76 F. Diederich and P. Rivera-Fuentes, *Angew. Chem., Int. Ed.*, 2012, **51**, 2818–2828.
77 V. O. Özçelik and S. Ciraci, *J. Phys. Chem. C*, 2013, **117**, 2175–2182.
78 N. Narita, S. Nagai, S. Suzuki and K. Nakao, *Phys. Rev. B: Condens. Matter Mater. Phys.*, 1998, **58**, 11009.
79 Q. Yue, S. Chang, J. Kang, S. Qin and J. Li, *J. Phys. Chem. C*, 2013, **117**, 14804–14811.
80 Q. Peng, W. Ji and S. De, *Phys. Chem. Chem. Phys.*, 2012, **14**, 13385–13391.

81 G. Wang, M. Si, A. Kumar and R. Pandey, *Appl. Phys. Lett.*, 2014, **104**, 213107.
82 X. Deng, M. Si and J. Dai, *J. Chem. Phys.*, 2012, **137**, 201101.
83 W. Wu, W. Guo and X. C. Zeng, *Nanoscale*, 2013, **5**, 9264–9276.
84 Z. Li, M. Smeu, A. Rives, V. Maraval, R. Chauvin, M. A. Ratner and E. Borguet, *Nat. Commun.*, 2015, **6**, 6321.
85 H. Yu, A. Du, Y. Song and D. J. Searles, *J. Phys. Chem. C*, 2013, **117**, 21643–21650.
86 B. Bhattacharya, N. B. Singh and U. Sarkar, *Int. J. Quantum Chem.*, 2015, **115**, 820–829.
87 J. Sarma, R. Chowdhury and R. Jayaganthan, *ACS Nano*, 2014, **9**, 1450032.
88 H. J. Hwang, J. Koo, M. Park, N. Park, Y. Kwon and H. Lee, *J. Phys. Chem. C*, 2013, **117**, 6919–6923.
89 J. Zhou, K. Lv, Q. Wang, X. S. Chen, Q. Sun and P. Jena, *J. Chem. Phys.*, 2011, **134**, 174701.
90 R. C. Andrew, R. E. Mapasha, A. M. Ukpong and N. Chetty, *Phys. Rev. B: Condens. Matter Mater. Phys.*, 2012, **85**, 125428.
91 J. Kang, J. Li, F. Wu, S. S. Li and J. B. Xia, *J. Phys. Chem. C*, 2011, **115**, 20466–20470.
92 Y. Jiao, A. Du, M. Hankel, Z. Zhu, V. Rudolph and S. C. Smith, *Chem. Commun.*, 2011, **47**, 11843–11845.
93 H. Bai, Y. Zhu, W. Qiao and Y. Huang, *RSC Adv.*, 2011, **1**, 768–775.
94 G. Luo, X. Qian, H. Liu, R. Qin, J. Zhou, L. Li, Z. Gao, E. Wang, W.-N. Mei, J. Lu, Y. Li and S. Nagase, *Phys. Rev. B: Condens. Matter Mater. Phys.*, 2011, **84**, 075439.
95 H. Bu, M. Zhao, H. Zhang, X. Wang, Y. Xi and Z. Wang, *J. Phys. Chem. A*, 2012, **116**, 3934–3939.
96 J. Zhou, K. Lv, Q. Wang, X. S. Chen, Q. Sun and P. Jena, *J. Chem. Phys.*, 2011, **134**, 174701.
97 N. Narita and S. Nagai, *Phys. Rev. B: Condens. Matter Mater. Phys.*, 1998, **58**, 11009–11014.
98 A. N. Enyashin and A. L. Ivanovskii, *Phys. Status Solidi B Basic Res.*, 2011, **248**, 1879–1883.
99 A. N. Enyashin and A. L. Ivanovskii, *Phys. Status Solidi B Basic Res.*, 2011, **248**, 1879–1883.
100 F. Molitor, J. Güttinger, C. Stampfer, S. Dröscher, A. Jacobsen, T. Ihn and K. Ensslin, *J. Phys.: Condens. Matter*, 2011, **23**, 243201.
101 K. Srinivasu and S. K. Ghosh, *J. Phys. Chem. C*, 2012, **116**, 5951–5956.
102 A. Ivanovskii, *Prog. Solid State Chem.*, 2013, **41**, 1–19.
103 D. Malko, C. Neiss and A. Görling, *Phys. Rev. B: Condens. Matter Mater. Phys.*, 2012, **86**, 045443.
104 T. Shao, B. Wen, R. Melnik, S. Yao, Y. Kawazoe and Y. Tian, *J. Chem. Phys.*, 2012, **137**, 194901.
105 X. Wei, B. Fragneaud, C. A. Marianetti and J. W. Kysar, *Phys. Rev. B: Condens. Matter Mater. Phys.*, 2009, **80**, 205407.
106 A. Bosak, M. Krisch, M. Mohr, J. Maultzsch and C. Thomsen, *Phys. Rev. B: Condens. Matter Mater. Phys.*, 2007, **75**, 153408.
107 Y. Y. Zhang, Q. X. Pei and C. M. Wang, *Appl. Phys. Lett.*, 2012, **101**, 081909.
108 A. Bosak, M. Krisch, M. Mohr, J. Maultzsch and C. Thomsen, *Phys. Rev. B: Condens. Matter Mater. Phys.*, 2007, **75**, 153408.
109 F. Liu, P. Ming and J. Li, *Phys. Rev. B: Condens. Matter Mater. Phys.*, 2007, **76**, 064120.
110 Y. Yang and X. Xu, *Comput. Mater. Sci.*, 2012, **61**, 83–88.
111 G. Hu, J. He, J. Chen and Y. Li, *J. Am. Chem. Soc.*, 2023, **145**, 5400–5409.
112 K. Tahara, T. Fujita, M. Sonoda, M. Shiro and Y. Tobe, *J. Am. Chem. Soc.*, 2008, **130**, 14339–14345.
113 E. L. Spitler, C. A. Johnson and M. M. Haley, *Chem. Rev.*, 2006, **106**, 5344–5386.
114 J. Zhong, J. Wang, J.-G. Zhou, B.-H. Mao, C.-H. Liu, H.-B. Liu, Y.-L. Li, T.-K. Sham, X.-H. Sun and S.-D. Wang, *J. Phys. Chem. C*, 2013, **117**, 5931–5936.
115 M. Ohkita, M. Kawano, T. Suzuki and T. Tsuji, *Chem. Commun.*, 2002, 3054–3055.
116 H. Du, Z. Deng, Z. Lü, Y. Yin, L. Yu, H. Wu, Z. Chen, Y. Zou, Y. Wang and H. Liu, *Synth. Met.*, 2011, **161**, 2055–2057.
117 J. Cai, P. Ruffieux, R. Jaafar, M. Bieri, T. Braun, S. Blankenburg, M. Muoth, A. P. Seitsonen, M. Saleh and X. Feng, *Nature*, 2010, **466**, 470–473.
118 J. Cai, C. A. Pignedoli, L. Talirz, P. Ruffieux, H. Söde, L. Liang, V. Meunier, R. Berger, R. Li and X. Feng, *Nat. Nanotechnol.*, 2014, **9**, 896–900.
119 P. Ruffieux, S. Wang, B. Yang, C. Sánchez-Sánchez, J. Liu, T. Dienel, L. Talirz, P. Shinde, C. A. Pignedoli and D. Passerone, *Nature*, 2016, **531**, 489–492.
120 F. Klappenberger, Y.-Q. Zhang, J. Björk, S. Klyatskaya, M. Ruben and J. V. Barth, *Acc. Chem. Res.*, 2015, **48**, 2140–2150.
121 B. Cirera, Y.-Q. Zhang, J. Björk, S. Klyatskaya, Z. Chen, M. Ruben, J. V. Barth and F. Klappenberger, *Nano Lett.*, 2014, **14**, 1891–1897.
122 Y.-Q. Zhang, N. Kepčija, M. Kleinschrodt, K. Diller, S. Fischer, A. C. Papageorgiou, F. Allegretti, J. Björk, S. Klyatskaya and F. Klappenberger, *Nat. Commun.*, 2012, **3**, 1286.
123 T. Wang, J. Huang, H. Lv, Q. Fan, L. Feng, Z. Tao, H. Ju, X. Wu, S. L. Tait and J. Zhu, *J. Am. Chem. Soc.*, 2018, **140**, 13421–13428.
124 H. Y. Gao, H. Wagner, D. Zhong, J. H. Franke, A. Studer and H. Fuchs, *Angew. Chem., Int. Ed.*, 2013, **14**, 4024–4028.
125 J. Liu, Q. Chen, L. Xiao, J. Shang, X. Zhou, Y. Zhang, Y. Wang, X. Shao, J. Li and W. Chen, *ACS Nano*, 2015, **9**, 6305–6314.
126 G. Fang and X. Bi, *Chem. Soc. Rev.*, 2015, **44**, 8124–8173.
127 Q. Sun, L. Cai, H. Ma, C. Yuan and W. Xu, *ACS Nano*, 2016, **10**, 7023–7030.
128 S. Zhan, X. Chen, B. Xu, L. Wang, L. Tong, R. Yu, N. Yang and D. Wang, *Nano Today*, 2022, **47**, 101626.
129 H. Liu, J. Xu, Y. Li and Y. Li, *Acc. Chem. Res.*, 2010, **43**, 1496–1508.
130 A. C. Ferrari, J. C. Meyer, V. Scardaci, C. Casiraghi, M. Lazzeri, F. Mauri, S. Piscanec, D. Jiang, K. S. Novoselov and S. Roth, *Phys. Rev. Lett.*, 2006, **97**, 187401.
131 L. Brillson, *Surf. Sci. Rep.*, 1982, **2**, 123–326.

132 X. Qian, H. Liu, C. Huang, S. Chen, L. Zhang, Y. Li, J. Wang and Y. Li, *Nature*, 2015, **5**, 7756.
133 J. Zhou, X. Gao, R. Liu, Z. Xie, J. Yang, S. Zhang, G. Zhang, H. Liu, Y. Li and J. Zhang, *J. Am. Chem. Soc.*, 2015, **137**, 7596–7599.
134 A. Zaman, A. Ghosh, S. Santra, J. Chakraborty, J. T. Orasugh and D. Chattopadhyay, in *Membranes for Water Treatment and Remediation*, ed. A. K. Nadda, P. Banerjee, S. Sharma and P. Nguyen-Tri, Springer Nature Singapore, Singapore, 2023, pp. 55–89, DOI: 10.1007/978-981-19-9176-9_3.
135 N. Banan Baghbani, J. Azamat, H. Erfan-Niya, S. Majidi and L. Khazini, *J. Mol. Graphics Modell.*, 2020, **101**, 107729.
136 J. Xu, K. Meng, Y. Niu, C. Zhang, K. Xu, J. Rong, Y. Wei and X. Yu, *Desalination*, 2023, **546**, 116183.
137 J. Li, Y. Chen, J. Gao, Z. Zuo, Y. Li, H. Liu and Y. Li, *ACS Appl. Mater. Interfaces*, 2019, **11**, 2591–2598.
138 X. Gao, J. Zhou, R. Du, Z. Xie, S. Deng, R. Liu, Z. Liu and J. Zhang, *Adv. Mater.*, 2016, **28**, 168–173.
139 A. H. Mashhadzadeh, A. M. Vahedi, M. Ardjmand and M. G. Ahangari, *Superlattices Microstruct.*, 2016, **100**, 1094–1102.
140 R. Liu, J. Zhou, X. Gao, J. Li, Z. Xie, Z. Li, S. Zhang, L. Tong, J. Zhang and Z. Liu, *Adv. Electron. Mater.*, 2017, **3**, 1700122.
141 Y. Li, H. Huang, R. Cui, D. Wang, Z. Yin, D. Wang, L. Zheng, J. Zhang, Y. Zhao, H. Yuan, J. Dong, X. Guo and B. Sun, *Sens. Actuators, B*, 2021, **332**, 129519.
142 X. Sun, M. Duan, R. Li, Y. Meng, Q. Bai, L. Wang, M. Liu, Z. Yang, Z. Zhu and N. Sui, *Anal. Chem.*, 2022, **94**, 13598–13606.
143 X. Guo, Y. Li, H. Huang, D. Wang, R. Cui, J. Li, Y. Zhao, D. Wang, H. Yuan, J. Dong and B. Sun, *J. Environ. Chem. Eng.*, 2022, **10**, 107159.
144 Y. Ai, L. Yan, S. Zhang, X. Ye, Y. Xuan, S. He, X. Wang and W. Sun, *Microchem. J.*, 2023, **184**, 108186.
145 J. Zhu, D. Liu, C. Li, B. Zhang, J. Wang, W. Wu, J. Ji and Y. Ma, *RSC Adv.*, 2021, **11**, 35408–35414.
146 S. Thangavel, K. Krishnamoorthy, V. Krishnaswamy, N. Raju, S. J. Kim and G. Venugopal, *J. Phys. Chem. C*, 2015, **119**, 22057–22065.
147 B. Song, M. Chen, G. Zeng, J. Gong, M. Shen, W. Xiong, C. Zhou, X. Tang, Y. Yang and W. Wang, *J. Hazard. Mater.*, 2020, **398**, 122957.
148 N. Yang, Y. Liu, H. Wen, Z. Tang, H. Zhao, Y. Li and D. Wang, *ACS Nano*, 2013, **7**, 1504–1512.
149 Y. Dong, Y. Zhao, Y. Chen, Y. Feng, M. Zhu, C. Ju, B. Zhang, H. Liu and J. Xu, *J. Mater. Sci.*, 2018, **53**, 8921–8932.
150 Y. Xue, Z. Zuo, Y. Li, H. Liu and Y. Li, *Small*, 2017, **13**, 1700936.
151 P. Kuang, B. Zhu, Y. Li, H. Liu, J. Yu and K. Fan, *Nanoscale Horiz.*, 2018, **3**, 317–326.
152 H.-Y. Si, Q.-X. Deng, L.-C. Chen, L. Wang, X.-Y. Liu, W.-S. Wu, Y.-H. Zhang, J.-M. Zhou and H.-L. Zhang, *J. Alloys Compd.*, 2019, **794**, 261–267.
153 L. Hui, Y. Xue, H. Yu, Y. Liu, Y. Fang, C. Xing, B. Huang and Y. Li, *J. Am. Chem. Soc.*, 2019, **141**, 10677–10683.
154 Y. Y. Han, X. L. Lu, S. F. Tang, X. P. Yin, Z. W. Wei and T. B. Lu, *Adv. Energy Mater.*, 2018, **8**, 1702992.
155 J.-X. Lv, Z.-M. Zhang, J. Wang, X.-L. Lu, W. Zhang and T.-B. Lu, *ACS Appl. Mater. Interfaces*, 2018, **11**, 2655–2661.
156 Y. Yao, Z. Jin, Y. Chen, Z. Gao, J. Yan, H. Liu, J. Wang, Y. Li and S. F. Liu, *Carbon*, 2018, **129**, 228–235.
157 Y. Fang, Y. Xue, L. Hui, H. Yu, Y. Liu, C. Xing, F. Lu, F. He, H. Liu and Y. Li, *Nano Energy*, 2019, **59**, 591–597.
158 L. Hui, D. Jia, H. Yu, Y. Xue and Y. Li, *ACS Appl. Mater. Interfaces*, 2018, **11**, 2618–2625.
159 L. Hui, Y. Xue, F. He, D. Jia and Y. Li, *Nano Energy*, 2019, **55**, 135–142.
160 Y. Xue, B. Huang, Y. Yi, Y. Guo, Z. Zuo, Y. Li, Z. Jia, H. Liu and Y. Li, *Nat. Commun.*, 2018, **9**, 1460.
161 G. Shi, C. Yu, Z. Fan, J. Li and M. Yuan, *ACS Appl. Mater. Interfaces*, 2018, **11**, 2662–2669.
162 H. Yu, Y. Xue, B. Huang, L. Hui, C. Zhang, Y. Fang, Y. Liu, Y. Zhao, Y. Li and H. Liu, *iScience*, 2019, **11**, 31–41.
163 X. Zhang, M. Zhu, P. Chen, Y. Li, H. Liu, Y. Li and M. Liu, *Phys. Chem. Chem. Phys.*, 2015, **17**, 1217–1225.
164 Q. Xu, B. Zhu, B. Cheng, J. Yu, M. Zhou and W. Ho, *Appl. Catal., B*, 2019, **255**, 117770.
165 Y. Xue, J. Li, Z. Xue, Y. Li, H. Liu, D. Li, W. Yang and Y. Li, *ACS Appl. Mater. Interfaces*, 2016, **8**, 31083–31091.
166 J. Zhang, Q. Bai, X. Bi, C. Zhang, M. Shi, W. W. Yu, F. Du, L. Wang, Z. Wang, Z. Zhu and N. Sui, *Nano Today*, 2022, **43**, 101429.
167 J. Zhu, S. Xiang, B. Zhang, J. Wang, C. Li, C. Pan, Y. Xu and Y. Ma, *J. Environ. Chem. Eng.*, 2022, **10**, 107724.
168 A. Shahali, M. Farahmand, H. A. Hussein, M. M. Kadhim, W. K. Abdelbasset, A. G. Ebadi and L. Wu, *Comput. Theor. Chem.*, 2022, **1209**, 113612.
169 Z. Zhang, Y. Muhammad, Y. Chen, S. J. Shah, Y. Peng, S. Shao, R. Wang, X. Li, H. Liu and Z. Zhao, *Chem. Eng. J.*, 2021, **426**, 131621.
170 H. Sajid, S. Khan, K. Ayub and T. Mahmood, *J. Mol. Model.*, 2021, **27**, 117.
171 S. Majidi, H. Erfan-Niya, J. Azamat, E. R. Cruz-Chú and J. H. Walther, *J. Mol. Graphics Modell.*, 2023, **118**, 108337.
172 F. Ai and J. Wang, *ACS Omega*, 2022, **7**, 31309–31317.
173 M. Yang, Z. Wang, D. Jiao, G. Li, Q. Cai and J. Zhao, *Appl. Surf. Sci.*, 2022, **592**, 153213.
174 J. Azamat, N. B. Baghbani and H. Erfan-Niya, *J. Membr. Sci.*, 2020, **604**, 118079.
175 D. Cohen-Tanugi, L.-C. Lin and J. C. Grossman, *Nano Lett.*, 2016, **16**, 1027–1033.
176 W. Xie, G. M. Geise, B. D. Freeman, H.-S. Lee, G. Byun and J. E. McGrath, *J. Membr. Sci.*, 2012, **403**, 152–161.
177 K. H. Lasisi, O. K. Abass, K. Zhang, T. F. Ajibade, F. O. Ajibade, J. O. Ojediran, E. S. Okonofua, J. R. Adewumi and P. D. Ibikunle, *Front. Chem.*, 2023, **11**, 1125625.
178 M. Raju, P. B. Govindaraju, A. C. Van Duin and M. Ihme, *Nanoscale*, 2018, **10**, 3969–3980.
179 C. Zhu, H. Li, X. C. Zeng and S. Meng, 2013, preprint, arXiv:1307.0208. DOI: 10.48550/arXiv.1307.0208.
180 M. Mehrdad and A. Moosavi, *Polymer*, 2019, **175**, 310–319.
181 J. Azamat, *Comput. Mater. Sci.*, 2021, **187**, 110118.

182 L. Zou, S. Zhang, J. Liu, Y. Cao, G. Qian, Y.-Y. Li and Z. P. Xu, *Environ. Sci. Pollut. Res.*, 2019, **26**, 34197–34204.
183 R. Epsztein, W. Cheng, E. Shaulsky, N. Dizge and M. Elimelech, *J. Membr. Sci.*, 2018, **548**, 694–701.
184 R. Liu, X. Gao, J. Zhou, H. Xu, Z. Li, S. Zhang, Z. Xie, J. Zhang and Z. Liu, *Adv. Mater.*, 2017, **29**, 1604665.
185 J. Zhou, Z. Xie, R. Liu, X. Gao, J. Li, Y. Xiong, L. Tong, J. Zhang and Z. Liu, *ACS Appl. Mater. Interfaces*, 2018, **11**, 2632–2637.
186 R. Matsuoka, R. Sakamoto, K. Hoshiko, S. Sasaki, H. Masunaga, K. Nagashio and H. Nishihara, *J. Am. Chem. Soc.*, 2017, **139**, 3145–3152.
187 C. Huang, Y. Li, N. Wang, Y. Xue, Z. Zuo, H. Liu and Y. Li, *Chem. Rev.*, 2018, **118**, 7744–7803.
188 J. Li, Z. Xie, Y. Xiong, Z. Li, Q. Huang, S. Zhang, J. Zhou, R. Liu, X. Gao and C. Chen, *Adv. Mater.*, 2017, **29**, 1700421.
189 J. Zhao, N. Wei, Z. Fan, J.-W. Jiang and T. Rabczuk, *Nanotechnology*, 2013, **24**, 095702.
190 S. Lin and M. J. Buehler, *Nanoscale*, 2013, **5**, 11801–11807.
191 D. Cohen-Tanugi and J. C. Grossman, *Nano Lett.*, 2014, **14**, 6171–6178.
192 M. Bartolomei and G. Giorgi, *ACS Appl. Mater. Interfaces*, 2016, **8**, 27996–28003.
193 M. Akhavan, J. Schofield and S. Jalili, *Phys. Chem. Chem. Phys.*, 2018, **20**, 13607–13615.